UNIVERSITÀ DEGLI STUDI DI PADOVA

Dipartimento di Fisica e Astronomia "Galileo Galilei"

Master Degree in Physics

Final Dissertation

Low-Energy Neutrino Astrophysics with Super-Kamiokande

Thesis supervisor

Prof. Gianmaria Collazuol

Thesis co-supervisor

Dr. Mathieu Lamoureux

Candidate

Marco Mattiazzi

Academic Year 2019/2020

Abstract

Core-Collapse Supernovae (CCSNe) are among the most powerful events in the cosmos where neutrinos play key role carrying away about 99% of the energy available. Despite the progress in the numerical studies the full details of the explosion mechanism are still unknown and only the novel observation of the neutrino burst from the next nearby CCSN will enable us to shed light on this phenomenon.

The Super-Kamiokande(SK) experiment is an underground water Cherenkov neutrino detector consisting in a very large volume cylinder filled with ultrapure water (50 kton) readout by about 11,000 photomultipliers and being located under 1,000m overburden of rock (2,700 m.w.e.).

SK is part of the Supernova Early Warning System (SNEWS), network which is coordinating most of the large-scale neutrino telescopes around the globe for the detection of such bursts, with a short latency. The current system at SK is designed to send normal warning if more than 25 events are detected within 20 seconds, which allows the efficient detection of the CCSNe up to the Small Magellanic Cloud. Offline analyses are also performed where only 7-8 events are required, allowing the extension of the search horizon up to few hundreads of kpc.

The main aim of the Thesis consists in exploring the differences between the time profiles of the SN neutrino signal and the standard poissonian background trend, in order to lower the current multiplicity thresholds of the real-time monitor, providing fast alerts within fixed false positive rate (1 false alarm per century).

To this purpose, new original statistical methods have been developed introducing additional cuts based not only on the absolute number of events but also on the characteristic time scale of the candidate SN clusters. The performances with different clustering algorithms have been tested as well.

Contents

List of Figures

Chapter 1

Introduction

Core-Collapse Supernovae (CCSNe) are among the most intriguing phenomena that occur in the cosmos, signalling the catastrophic end of massive stars. The violent explosions are supposed to be neutrino-driven, since these elusive particles are able to carry away about 99% of the released energy ($\sim 10^{53}$ erg). In this Thesis I approached the neutrino physics of core-collapse supernovae (CCSNe) within the Super-Kamiokande Experiment in Japan. The subject is of great interest both from an experimental and a theoretical point of view.

The theory of CCSNe is not yet fully understood and a plethora of complex multidimensional simulations have been developed by several groups of theoreticians around the world. Despite the lack of universal consensus on the physics ruling such phenomenon, the large emission of MeV neutrinos during the explosion is well-established as confirmed by the SN1987A observation, altough it is the only experimental measurement, so far.

The detection of high-statistics neutrino signal from the next nearby CCSN is therefore of paramount importance because it will provide deep insight into the SN physics where the unique interplay between particle physics, astrophysics, and nuclear physics is available. Namely, just a single new detection of neutrino burst with the current facilities, would allow us to:

- provide neutrino mass limit through the time-of-flight delay with respect to the SN light observation;
- shed light on the neutrino mass hierarchy,*e.g.* via the rise time shape of the neutronization burst (first stage of the SN neutrino spectrum) or through the ratio of the SN neutrino charged current and neutral current interaction rates in scintillation detectors;
- guide the optical telescopes to study the SN light signal from its onset;
- have unique probe for black-hole forming SN (or other hypothetical "*failed*" explosions) which have no (or very faint) electromagnetic counterpart;
- perform a multi-messenger detection along with gravitational waves supplying comprehensive picture of the catastrophic phenomenon;
- clarify the role of SN neutrinos in the nucleosynthesis of trans-iron elements;
- establish a new standard candle method to evaluating SN distance by means of the neutronization burst;
- set constraints on new physics since, new particles (*e.g* right-handed neutrinos, axions,etc.) are expected to emerge from non-standard cooling mechanisms [1] and the exotic neutrino features (*e.g.* decays, charge,...) are supposed to distort the SN neutrino flux;
- demonstrate the hydrodynamical instabilities, predicted by recent numerical studies, which provide fundamental inputs for successful explosions (in the *delayed neutrino-driven scenario*).

[1] *e.g.* the last stage of SN neutrino spectrum should deviate from the predicted duration

Additionally, the non-detection period by neutrino telescopes enable us to estimate the galactic SN rate in a further independent way.

The Super-Kamiokande is currently the largest underground water Cherenkov detector in the world. In this thesis work I have investigated possible enhancements to the real-time SN monitor operating at Super-Kamionkade.

In Chapter 2, an introduction to the state of the art for the theory of CCSNe is outlined with the main focus on the expected neutrino signal spectrum and the available large-scale detectors able to reveal it in real-time.

In Chapter 3, the general description of the Super-Kamiokande detector is presented with a special attention on the low-energy neutrino event reconstruction machinery.

In Chapter 4, the real-time SN monitor operating at Super-Kamiokande is described and the current SN alert system is motivated.

In Chapter 5, new original statistical methods are developed exploiting the differences between the time profile of SN neutrino signal and the standard poissonian background component with the aim of extending the horizon visible in real-time.

In Chapter 6, the problem of the non-poissonian component of the SK background is approached and, after reviewing the current techniques, a new method based on the average nearest neighbor distance, is proposed and some preliminary studies are performed.

Chapter 2

Neutrinos from Core-Collapse Supernovae

2.1 Synopsis of Core-Collapse Supernova Physics

The Core-Collapse SuperNovae (CCSNe) is the last stage of the lifecycle of the massive stars ($M_{ZAMS} > 8M_{\odot}$) leading to a neutron star or to a black hole. The energy released during this explosion is[1] $\sim 10^{53}$erg, making it one of the most powerful phenomenon in the cosmos.

In contrast to thermonuclear SN explosion[2] where neutrino emission is negligible, the role of neutrinos in CCSNe is crucial since these particles carry away almost the 99% of the available gravitational energy due to their weakly-interacting nature.

The evolution phases leading from the massive star to the compact object, are illustrated in figure 2.1 and summarized in the following sections. More details on some of the current CCSN models can be found in[20],[21], [18],[8] [31].

2.1.1 Pre-Collapse phase

The massive star has the so-called *onion shell* structure, displayed in figure 2.2, where the different nuclear burning stages, except the iron core, supply the additional energy needed to ensure the hydrostatic equilibrium via the fusion reactions.

The inert iron core, with radius of $\sim 10^3$ km, is supported, mainly, by the *electron degeneracy pressure* instead.

2.1.2 Onset of the collapse

When the Chandrasekhar mass limit ($\sim 1.4M_{\odot}$) is reached, the core, being gravitational unstable, starts to collapse, actually on free-fall time scale. Since other sources of energy are not available, the core contraction speeds up increasing its temperature. As the density grows up, two other processes boosts the core compression reducing the electron degeneracy pressure:

- the iron photodisintegration
$$\gamma + {}^{56}_{26}\mathrm{Fe} \longleftrightarrow 13\,{}^{4}_{2}\mathrm{He} + 4\mathrm{n}$$
- the electron capture (EC) reactions
$${}^{56}_{26}\mathrm{Fe} + e^- \rightarrow {}^{56}_{25}\mathrm{Mg} + \nu_e$$
$${}^{56}_{25}\mathrm{Mg} + e^- \rightarrow {}^{56}_{24}\mathrm{Cr} + \nu_e$$

[1] an approximate calculation can be made knowing the mass and the radius of the remaining neutron star. Indeed if the compact object is assumed as an homogeneous sphere, governed by Newtonian gravity, the gravitational energy can be evaluated as
$$U_g = \frac{3}{5}\frac{G\,M_{ns}^2}{R_{ns}} \approx 3.6 \times 10^{53} \left(\frac{M_{ns}}{1.5M_{\odot}}\right)^2 \left(\frac{R_{ns}}{10\mathrm{km}}\right)^{-1} \mathrm{erg}$$

[2] if the progenitor mass is $4M_{\odot} < M_{ZAMS} < 8M_{\odot}$

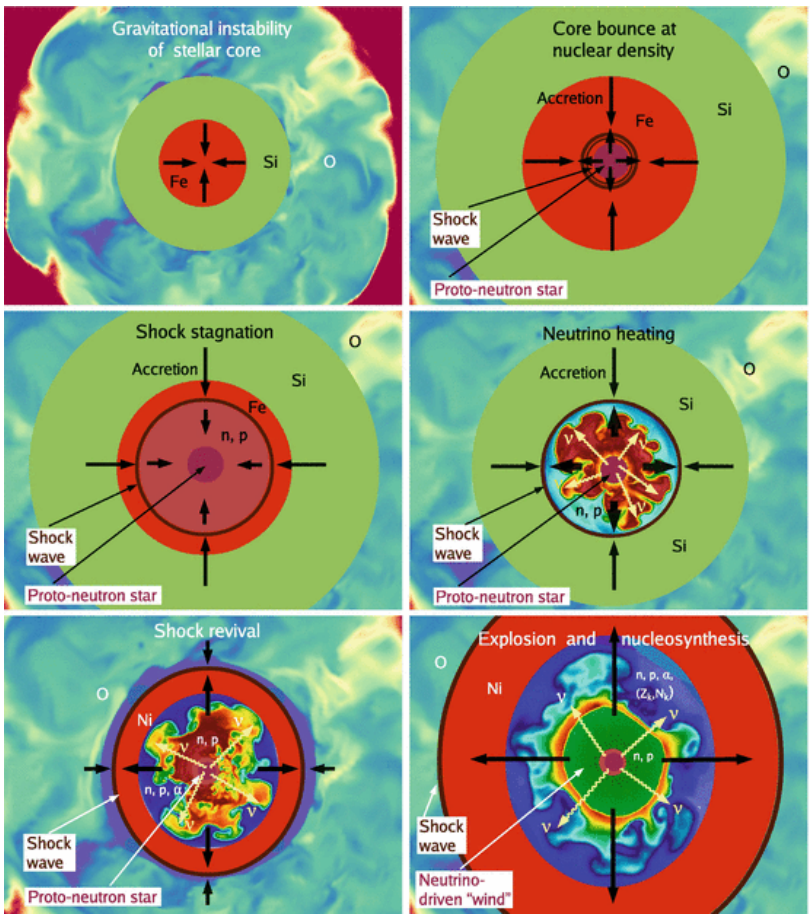

Figure 2.1: Schematic of the CCSN phases in the *delayed neutrino-driven* scenario. Figure from[21]

As the core density reaches[3] $\rho \approx 10^9$ g cm^{-3} , the EC reactions occur, enhancing the neutronization of the core. It is worth mentioning that the electron neutrinos escape almost unhindered in this phase.

2.1.3 Neutrino trapping phase

As the density overcomes $\approx 10^{11}$ g cm^{-3} the neutrinos start to diffuse since its mean free path, mainly due to NC neutrino coherent scattering on heavy nuclei

$$\nu + (\mathrm{A}, \mathrm{Z}) \longleftrightarrow \nu + (\mathrm{A}, \mathrm{Z}) \tag{2.1}$$

has become smaller than the radius of the collapsing core($\lesssim 10$ km).

The neutrino diffusion, in the so-called *neutrinosphere*[4] , provides additional pressure but it is not enough to arrest the collapse.

2.1.4 Core bounce and Shock propagation

As the core reaches the nuclear matter density $\rho_{nucl} \sim 2.4 \times 10^{14}$ g cm^{-3} , the repulsive component of the strong force potential comes into play bouncing off the in-falling core and generating outward-travelling shock wave.

As the shock wave begins to expand outward it interacts with the still in-falling matter. The kinetic energy of the latter is converted into thermal energy that heats up the post-shock medium enabling the complete iron photodisintegration into unbound neutrons and protons.

This process dissipates sizable amount energy[5] slowing down the shock. Further energy is consumed by the electron neutrinos produced via EC onto the free protons of the shock-heated plasma. These

[3] *i.e.* thermal energy of several MeV.

[4] the *radius* of the neutrinosphere is defined as the average distance travelled by neutrino before escaping freely.

[5] 1.7×10^{51} erg per 0.1 $M_\odot$ matter crossed, this educated guess can be found in [20].

Shell structure of pre-SN massive star

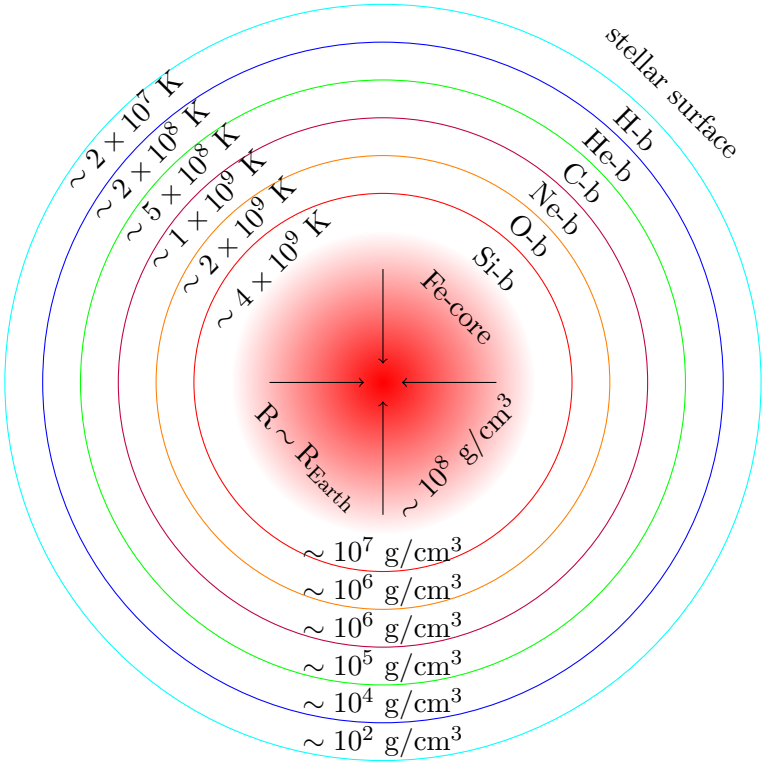

Figure 2.2: Schematic of the structure of pre-SN Fe-core massive star.

neutrinos are initially trapped in the high-density medium behind the outward-moving shock, but as the density of the outer layers decreases up to $\rho_{nucl} \lesssim 10^{11}\ \mathrm{g\,cm^{-3}}$, and the neutrino diffusion becomes faster than the shock front allowing the sudden emission of the electron neutrinos.

This, so-called ν_e *neutronization burst*, occurs at $\mathcal{O}(10)$ ms after the core bounce when the shock begins to stall still inside the collapsing iron core[6] without[7] triggering the explosion (the *delayed neutrino-driven* scenario). Now, the shock is turned into an *accretion* shock.

2.1.5 Shock revival

After the *prompt shock* is ceased, the proto-neutron star(PNS) begins to contract and the gravitational energy is carried away by neutrinos of all flavours but with different ratios, accordingly to the available production channels.

As matter of fact muon and tau neutrinos and antineutrinos, also grouped together as ν_x in the CCSN literature, are produced in the denser layers via electron positron pair, nucleon-nucleon bremsstrahlung, and neutrino pair annihilation, respectively

$$e^+ + e^- \longrightarrow \nu + \bar{\nu} \tag{2.2}$$

$$\mathrm{N} + \mathrm{N} \longrightarrow \mathrm{N} + \mathrm{N} + \nu + \bar{\nu} \tag{2.3}$$

$$\nu_e + \bar{\nu}_e \longrightarrow \nu_x + \bar{\nu}_x \tag{2.4}$$

whereas for electron neutrinos and antineutrinos the EC modes[8] provide further cooling channels to the nascent neutron star.

[6] radius of about 150 km and enveloped in a mass of around 1 $M_\odot$

[7] it is worth reminding that the exact mechanism of CCSN explosion is still unknown. Hence, all the available models are based on highly sophisticated multi-dimensional simulations which, inevitably, rely on approximation schemes due to the extreme environment and the complexity of the involved physics.

[8] the EC channels are $e^- + p \to n + \nu_e$ and $e^+ + n \to p + \bar{\nu}_e$

As demonstrated by the recent SN simulations [21], the continuous injection of new energy by neutrinos in the layers between neutrinosphere and the accretion shock via, mainly[9], the CC reactions

$$\nu_e + n \rightarrow p + e^-$$
$$\bar{\nu}_e + p \rightarrow n + e^+$$

can rejuvenate the expansion of the stalled shock due to the fact that only a small fraction ($\sim 1\,\%$) of the total gravitational energy released is required to drive the shock out of the collapsing core.

Additionally to the described *neutrino-heating mechanism*, the numerical multi-dimensional investigations[10] display the shock revival can be corroborated, enough to initiate the explosion, by the highly non-linear motion due to hydrodynamic instabilities [11] , especially for massive progenitors.

However, after the explosion, the PNS accretion is not powered off but it still proceeds, in parallel to the shock expansion, on a time scale $\mathcal{O}(100)$ ms depending, essentially, on the progenitor features.

2.1.6 PNS cooling phase

At the end of the accretion phase the PNS enters to the Kelvin-Helmoltz cooling phase. The residual binding energy is dissipated via the emission of neutrinos of all flavours, almost with the same luminosity. However these neutrinos can also transfer energy in the cooler layers above the PNS surface (the so-called *neutrino-driven wind*) enabling the nucleosynthesis of trans-iron elements.

As pointed out by [7], the time scale of this phase is ruled by neutrino diffusion and it is $\mathcal{O}(10)$ seconds.

2.2 The Supernova neutrino spectrum

In the case of the next high-statistics CCSN detection, the neutrino spectrum would provide deep insight into the involved multi-sectoral physics enabling the discrimination between different SN models[30]. Indeed the neutrinos from CCSNe can be viewed as unique probes to investigate SN central engine inaccessible to the optical observations.

Accordingly to the description of the section 2.1, the neutrino signal can be classified into three stages : ν_e *neutronization burst*, *accretion* and *cooling* stages.

The simulated neutrino spectrum for progenitor mass of $20M_\odot$ and metallicity Z = 0.02 is illustrated in the figure based on the model[33].

2.2.1 Neutronization burst

The neutronization burst(NB) stage is characterized by the rapid emission of ν_e in $\mathcal{O}(10)$ ms post-bounce. The energy released is $\sim 10^{51}$ erg and the peak is reached at ~ 2 ms with maximal luminosity $\approx 10^{53}$ erg/s .

Despite the energy involved is only 1% of the total, the NB detection would furnish precious information because it is independent on the progenitor mass and on nuclear equation of state. Thus, as reported in [22], it might be used as new *standard candle* for the SN distance estimation with a precision of 5%. It is worth emphasizing that this method would be the only one able to extract such distance in the case of optical obscured SN.

Additionally, the time evolution of the NB spike is sensitive to the neutrino mass hierarchy [44][22].

In parallel to the ν_e blast, there is the rise of heavy-flavour neutrino luminosity, which are thermally generated in the high-temperature deepest layers, and, with short delay, the steeper rise of $\bar{\nu}_e$ flux.

As the ν_e luminosity reaches its plateau and becomes comparable to $\bar{\nu}_e$ luminosity (it is slightly higher due to the neutronization of the core), the NB phase ends opening the accretion stage.

[9] the ES contributes to the heating of outer layers as well.

[10] *i.e.* beyond the spherical symmetry. Despite the high complexity, the 2D and 3D simulations are the only ones that can produce successful explosions without artificial inputs, so far.

[11] like convective motion, standing accretion shock instability (SASI), lepton emission self-sustained asymmetry (LESA), etc. For more details see *e.g.* [8] [44]

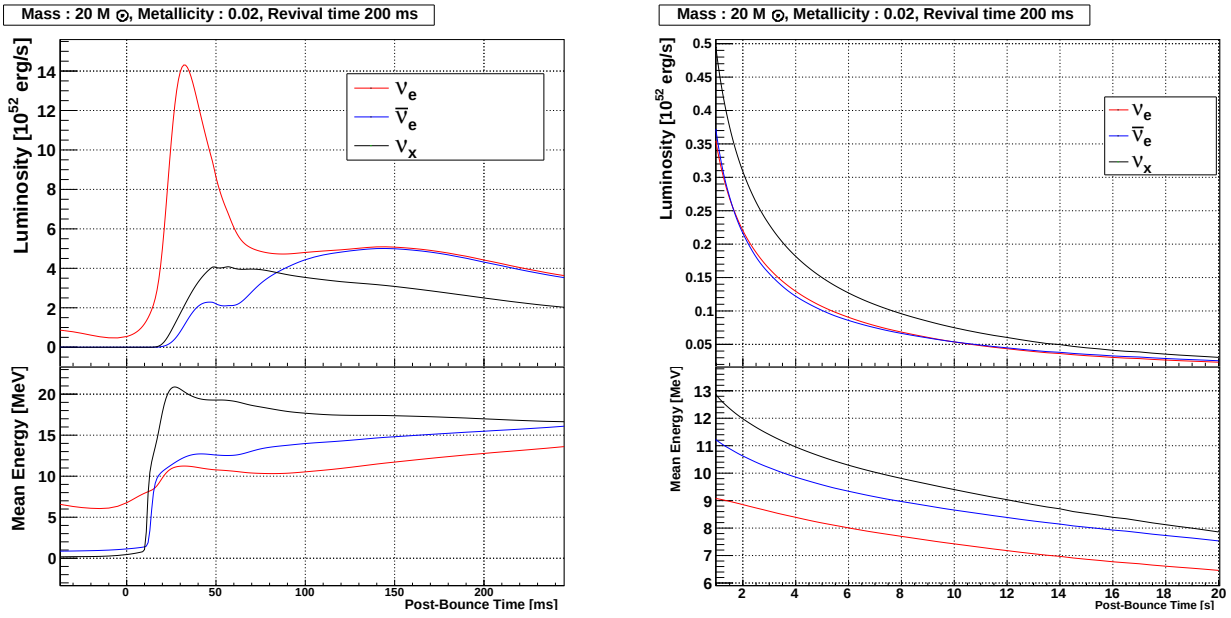

Figure 2.3: Simulated CCSN neutrino spectrum of 20 $M_{\odot}$, Z=0.02 and t_{revive} = 200 ms, based on [33] model from data available on Supernova Neutrino Database. (*Top*) Luminosity, (*Bottom*) Mean energy as function of time. (*Left*) the neutronization burst and the accretion phases , (*Right*) the cooling phase.

2.2.2 Accretion phase

The accretion phase is strongly dependent on the initial conditions[12] and on the models.

In fact the description of the neutrino-heating mechanism requires the solutions of the neutrino transport equations which can be achieved only via approximation schemes due to the complexity and the uncertainties of the physics involved. However common features have been found between the results of the different groups of theoreticians and can be summarized as follows

- the luminosity $\mathcal{L}\nu_x$ is about half of $\mathcal{L}\nu_e \approx \mathcal{L}\bar{\nu}_e$ because muonic and tauonic neutrinos can be generated only via NC interactions deep inside of the collapsing star;
- average *energy hierarchy* is $\langle E\nu_e \rangle < \langle E\bar{\nu}_e \rangle < \langle E\nu_x \rangle$ since the heavy flavour neutrinos decouple earlier(as consequence of the lack of CC modes) in the SN layers where the temperatures are highers. The difference between ν_e and $\bar{\nu}_e$ are due to the ongoing neutronization of the core instead;
- the flavour ratio of the emitted neutrinos is dependent on the mass accretion rate $M_{acc}(t)$ and on the PNS growing mass $M_{NS}(t)$;
- as general trend, the average energy increases almost proportionally to the PNS growing rate with a flavour-dependent constant;
- the hydrodynamic instabilities that cause large-scale oscillations of the accretion rate can leave clear signature via quasi-sinusoidal modulation in part of the related spectrum[13].

As the luminosities for all neutrino species approach almost the same magnitude, the accretion phase ends[14] (it lasts $\lesssim$ 1s) and the cooling phase begins.

[12] mainly, the progenitor mass.

[13] the future large-scale water Cherenkov detector Hyper-Kamiokande is the most promising since it will be able to resolve this part of the spectrum on event-by-event basis with the highest resolution, whereas in IceCube these modulations (and, in general,the entire SN neutrino signal spectrum) will be superimposed to the dominant background.

[14] in the 1D spherical simulation the accretion stage is abruptly terminated as the explosion occurs, whereas in the multi-dimensional scheme there is smooth transition between the two phases .

2.2.3 Cooling phase

In this phase the outer layers of the PNS are cooled by neutrino emission. Hence, the average energies for all type of neutrinos start to decrease.

After reaching almost the same value, within $\sim 10\%$, all luminosities $\mathcal{L}_{\nu_i}$ decline in a quasi-stationary fashion depending on the PNS features.

This part of neutrino spectrum can therefore enable us to set constraints on the nuclear equation of state and on the PNS mass and radius depending on the cooling timescale.

2.2.4 Black-hole forming scenario

In the case of the neutrino-heating mechanism, corroborated by the hydrodynamic instabilities, is not powerful enough to initiate the SN explosion, a black hole is formed instead of a neutron star.

The detectable signature of BH-forming scenario is sharp end of the neutrino light curve at $\mathcal{O}(500)$ ms post-bounce but with the same total energy released $\approx 10^{53}$ erg.

Lastly, as suggested in [18], the higher number of emitted neutrinos in shorter time compared to standard CCSN could allow us to extend the standard horizon of the future Megaton neutrino telescopes, which are supposed to observe SN neutrino on yearly basis.

2.2.5 The SN1987A observation

On 23 February 1987 at 7:35 UT, the first and the only detection of 24 astrophysical neutrinos from SN was achieved [6]. The explosion, occured in the Large Magellanic Cloud (LMC) at about 50 kpc, was clearly recorded almost simultaneously by the two large water Cherenkov detectors, Kamiokande II [17] and IMB [15], and by the scintillator detector Baksan [3], marking the dawn of the neutrino astronomy.

Despite the small statistics[15] of the data sample, the timing and energy distributions confirmed the essential picture of the CCSN theory in the delayed scenario. The acquired spectra are illustrated in figure 2.4 and one can appreciate that:

- the neutrino bursts last for ~ 10 s, consistently with the expected time scale of the PNS *cooling* phase. In addition it has two-step structure where the duration of the first stage is compatible with the *accretion* phase;
- the energy distribution of the cooling phase is, consistently, decreasing;
- the detected *fluences*[16] agree with the estimated ($\sim 10^{53}$ erg) energy released by the gravitational core-collapse of the massive star and with the formation of $1.4M_{\odot}$ (and $R_{NS} = 15$ km) neutron star.

On the particle physics side it shed light on some neutrino properties,which are briefly summarized as follows:

- 10 eV upper bound on the neutrino mass from the arrival time distribution[38];
- within 2 ppb the neutrino velocity limit is consistent with the speed of light[42];
- constraints on the possible exotic neutrino features (*e.g.* magnetic moment[5] and decay time[11] and on *non-standard* cooling scenarios due to BSM physics[9].

Moreover the neutrino signal reached the Earth some hours before the electromagnetic counterpart due to its weakly-interacting nature, although the search for neutrino bursts was performed after the optical observation .

[15] 11, 8, 5 SN neutrino signals were detected by Kamiokande II, IMB and Baksan respectively. The sensible volumes were 2.2 kton and 5 kton for Kamiokande II and IMB, but for the latter, the higher energy threshold (~ 20 MeV) caused smaller detection efficiency.

[16] *fluence* is defined as the neutrino flux $\Phi_\nu(E,t)$ integrated over the burst time.

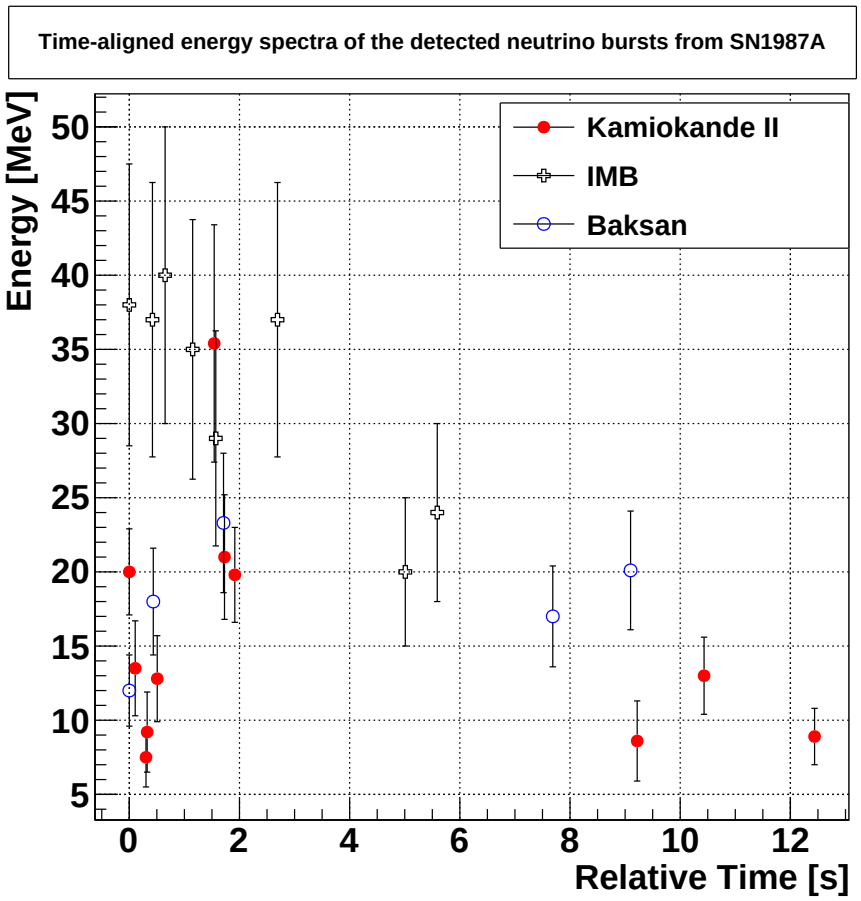

Figure 2.4: The time evolution along with the energy distribution of the SN1987 neutrino bursts detected at Kamiokande II, IMB and Baksan. It is worth mentioning that the first event of each detector is assumed as starting point because the synchronization among neutrino telescopes was not available at the time. The data are taken from [17], [15], and [3].

Thus, this feature can be exploited to generate prompt alert in the case of the next nearby CCSN, provinding the possibility to investigate the SN light curve from its onset. In this regard the SuperNova Early Warning System (SNEWS) has been developed as it shall be described in the next section.

2.3 Supernova neutrino detectors

Despite the enormous progresses made in numerical modelling of CCSNe, only the next detection may permit us to shed light on the fine details of this phenomenon. As reported in [16], the ideal SN neutrino detector should provide:

- low energy threshold and low background;
- sensitivity to all the flavour components ν_e, $\bar{\nu}_e$, ν_x;
- good timing resolution;
- large active volume ($\sim$ Mton) to perform high-statistics detection[17] in the case of the next event in our galaxy, and, potentially, to reach farther galaxies;
- high duty cycle since the galactic SNe are rather rare ($\sim$ 1/60 years according to [37]) ;
- good angular resolution with short latency to carry out multi-messenger detection along with the electromagnetic signal.

[17] especially in the ν_e neutronization burst region of the spectrum as seen in 2.2.1

Since current large volume neutrino detectors are primarly designed with other scientific aims, no one can satisfy all the requirements. Thus, the synchronization of the available neutrino telescopes is essential.

2.3.1 SuperNova Early Warning System

The SuperNova Early Warning System (SNEWS) is a world-wide network of seven SN neutrino detectors : Super-Kamiokande (Japan), LVD (Italy), Ice Cube (South Pole), KamLAND (Japan), Borexino (Italy) Daya Bay (China), and HALO (Canada); that can broadcast real-time warnings if a candidate SN event is found.

The SNEWS main aim consists of providing prompt alerts to astronomers in the case of the next galactic CCSNe with low false alarm rate (fixed to one fake warning per century).

The full design specifications are described in [4][39]. In summary, each detectors send blind datagrams to central coincidence server located at Brookhaven National Laboratory(BNL). If a single experiment finds a SN candidate, the bulletin could be flagged as GOOD or POSSIBLE, based on experiment-dependent criteria. Afterwards, if at least two detectors are triggered within 10 seconds, the SNEWS protocol for outputting automatic alerts (GOLD labelled) requires the following conditions on two or more experiments:

- GOOD flags, with the average rate of GOOD alerts in the previous time windows below some fixed thresholds based on Poisson statistics;
- being located in different area of the world;

Otherwise the coincidence signal is referred to as SILVER and it requires human-checking between collaborators before making any global warning.

It is worth pointing out that the coincidences between two or more telescopes allow us to:

- reduce the number of false positive alerts with respect to stand-alone SN monitors. A further improvement is related to reduction of the so-called *non-poissonian*[18] background being present in every detectors and difficult to reject in real-time;
- point the SN event in the sky via prompt triangulation enabling the optical observation of SN from its onset. Now, this method is not feasible due to the short latency constraint but it should be with the future large volume neutrino telescopes, as reported in [28]. It is worth mentioning that, currently, the only way to extract SN direction is from neutrino-electron scattering interactions in the Super-Kamiokande water Cherenkov detector.

Lastly, in this Thesis I shall focus on the Super-Kamiokande online SN monitor with the primary objective of extending the current horizon visible in real-time, and, simultaneously, ensuring the required false positive rate[19]. However, before entering to the technical description of the developed statistical methods, the understanding of Super-Kamiokande detector is needed and, therefore, the next chapter 3 shall be devoted to it.

[18] in the SN online analysis, the background is assumed to follow Poisson distribution with constant rate. Any cluster of events that is not classifiable on this basis and it is not SN signal, is referred to as *non-poissonian*. As we shall see 6, this component is critical in the Super-Kamiokande experiment.

[19] 1 fake event per century.

Chapter 3

The Super-Kamiokande detector

3.1 Overview of Super-Kamiokande detector

Super-Kamiokande (SK) is an underground water Cherenkov neutrino detector located at latitude 36°25'N and longitude 137°18'E in a cavity of the Kamioka mine under the peak of Mt.Ikenoyama. The 1,000 meters (2,700 m.w.e.) overburden of rock enables 5 orders of magnitude reduction of the down-going cosmic ray muons, that pass through SK at $\sim$ 2.2 Hz rate.

The SK consists of large volume tank with cylindrical shape (39 m diameter and 42 m height) filled with ultra-pure water (50 kton) readout by very sensitive PMTs (dynamic range from 1 to 300 photoelectrons). Inside the tank, 55 cm thick barrier divides SK into two concentric and optically isolated volumes: the *inner detector* (ID) readout by $\sim 11,100$ inward-facing 20-inch PMTs that actually covers [1] $\approx 40\%$ of the surface area of the (32.5 kton) inner volume; an *outer detector*(OD), readout by 1,885 outward-facing 8-inch PMTs, that works as *veto* for CR muons and shower-induced secondary particles as well as from environmental radiation (neutrons and gamma rays) caused by the nearby rocks. The official schematic is illustrated in figure 3.1.

The scientific objectives of the SK experiment[13] include proton decay search and the studies of neutrinos from cosmic and man-made sources. In detail the wide dynamic energy range (from few MeV up to $\mathcal{O}(1)$ TeV) make it an ideal detector for investigating SN neutrinos.

3.2 Cherenkov radiation

SK detects the charged lepton produced by neutrino interaction by means of Cherenkov effect in water. The Cherenkov radiation is emitted when a charged particle travels through the medium faster than the speed of light in the medium itself. The energy threshold for the Cherenkov light emission depends on the mass of the charged particle m and on the refractive index[2] $n(\lambda)$, as

$$\frac{E_t}{m} = \frac{n}{\sqrt{n^2 - 1}}$$

In water the energy thresholds are 0.77, 157.4 and 207.9 MeV for electrons, muons and pions, respectively.

Additionaly the Cherenkov light is radiated along a cone with an angle given by

$$\cos\theta_C = \frac{1}{\beta\, n}$$

where β is the speed of the charged particles. In the case of ultra-relativistic particles (like most of the electrons and muons at SK) passing through water the Cherenkov angle is ≈ 42 °.

[1] the other areas are covered with black sheets to avoid undesired reflections and to optically isolate the ID and the OD as much as possible.

[2] which it depends, in turn, on the Cherenkov photon wavelength.

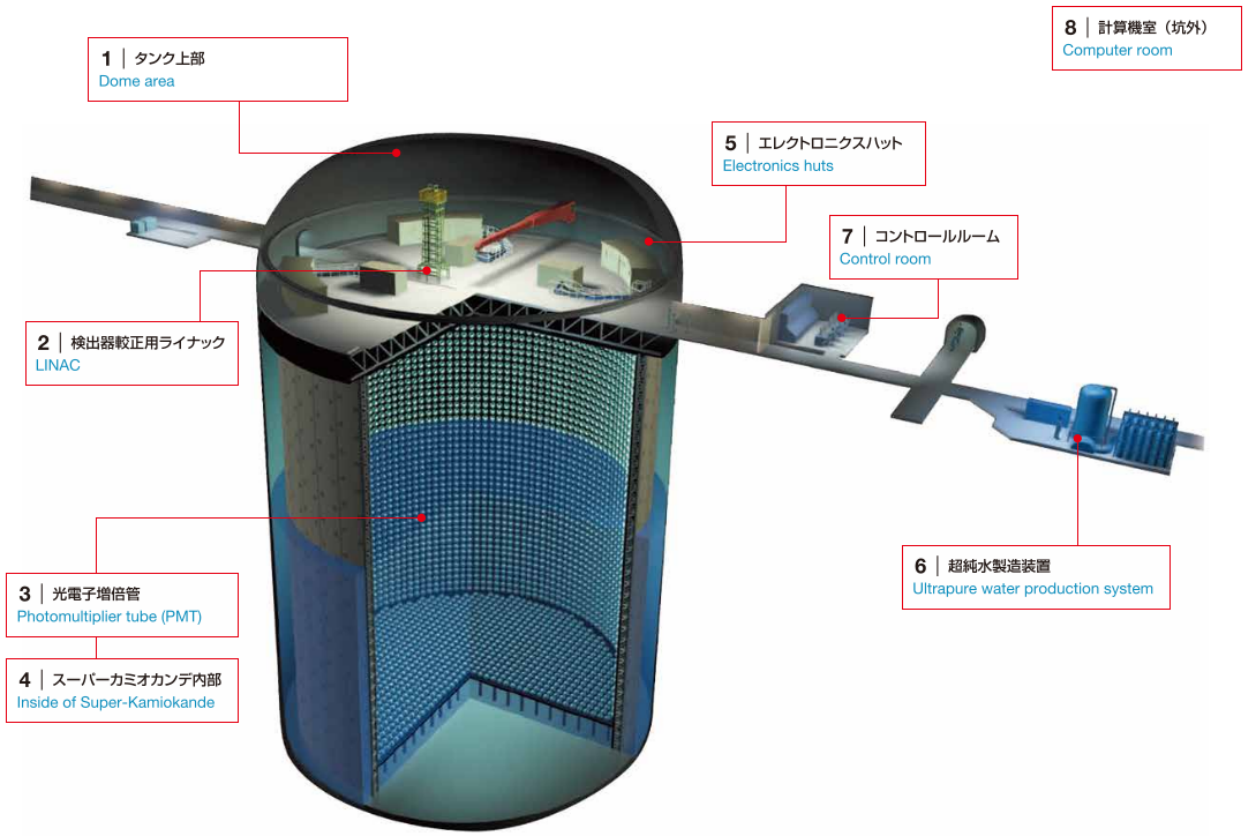

Figure 3.1: The layout of the Super-Kamiokande detector. Figure from the brochure available on the SK official site.

The number of Cherenkov photons emitted per unit length x and per unit wavelength λ for particle with charge ze follows

$$\frac{d^2N}{dx\,d\lambda} = \frac{2\pi\alpha z^2}{\lambda^2}\left(1 - \frac{1}{\beta^2 n_\lambda^2}\right) \sim \frac{1}{\lambda^2} \tag{3.1}$$

In the SK case the estimation of the Cherenkov photons is performed integrating in the interval $[300, 600]$ nm, which is the PMT dynamic range.

The effective number of detected photons depends on the Cherenkov light propagation in water. The light intensity in water is ruled by

$$I(x) = I_0(\lambda)e^{-\frac{x}{L(\lambda)}}$$

where $L(\lambda)$ is the *water transparency*[3] which is evaluated by means of laser calibrations and it consists of the sum of three terms

$$L(\lambda) = \frac{1}{\alpha_{\text{absorption}}(\lambda) + \alpha_{\text{Rayleigh}}(\lambda) + \alpha_{\text{Mie}}(\lambda)} \tag{3.2}$$

$$= \frac{1}{\alpha_{\text{absorption}}(\lambda) + \alpha_{\text{symmetric}}(\lambda) + \alpha_{\text{asymmetric}}(\lambda)} \tag{3.3}$$

where the coefficients due to Rayleigh and Mie scatterings are also grouped together in the symmetric (mainly Rayleigh) and asymmetric (mainly Mie) scattering components that are easier to discriminate experimentally.

[3] also referred to as *light attenuation*. The control of this quantity is crucial in the energy reconstruction since it is one of the main source of systematic uncertainties.

3.3 Interaction channels in water detectors

The astrophysical neutrinos impinging on the active volume of the detector might interact both via CC and NC processes. However the neutrino detectors, independently on its nature, allow us to measure only the properties of the lepton involved in the interaction.

In the SN energy region (tens of MeV), the CC interactions with ν_μ and ν_τ are forbidden due to the intrinsic thresholds of the processes. Hence, the SN neutrinos with such flavours can only be detected through the product of NC interactions.

The available interactions channels and their relative strengths for SN neutrinos are strongly dependent on the type of neutrino telescope. In the case of water Cherenkov detectors, like SK and the planned HK, the dominant channels are:

- **inverse beta decay**

$$\bar{\nu}_e + p \rightarrow e^+ + n$$

  is the main channel ($\sim 90\,\%$) in water due to the richness of free protons in this environment. In addition the energy threshold is quite low(1.8 MeV) and the detectable positron energy enable us to reconstruct the $\bar{\nu}_e$ energy, although the information on direction is lost.

- neutrino-electron **elastic scattering**

$$\nu_{e,x} + e^- \rightarrow \nu_{e,x} + e^-$$

  proceeds both through the NC and the CC processes. It is sensitive to all flavours but the cross section is about two order of magnitude smaller than IBD. Nevertheless this channel plays crucial task in the SN alert system because the scattered electron preserve the directional information of the incoming neutrino within 30 °.

- **charged current** oxygen channels

$$\nu_e + {}^{16}\mathrm{O} \rightarrow e^- + \mathrm{X}, \qquad \bar{\nu}_e + {}^{16}\mathrm{O} \rightarrow e^+ + \mathrm{X}$$

  have higher energy thresholds $\mathcal{O}(10)$ MeV and several final states (de-excitation γ_s, nucleons, etc.) are populated as reported in [23]. Despite the expected low event rates, its precise estimation[4] might allow us to discriminate between different SN models because the variations(depending on the neutrino oscillation hypothesis as well) are up to two order of magnitudes [30].

The cross sections for the described interaction channels are summarized in figure 3.2. The typical relative strengths of the SN neutrino interaction modes at Super-Kamiokande are displayed in the pie chart 3.3.

[4] viable at SK only in the case of very close high-statistics CCSN detection. In this respect, it will be more promising the future Hyper-Kamiokande detector.

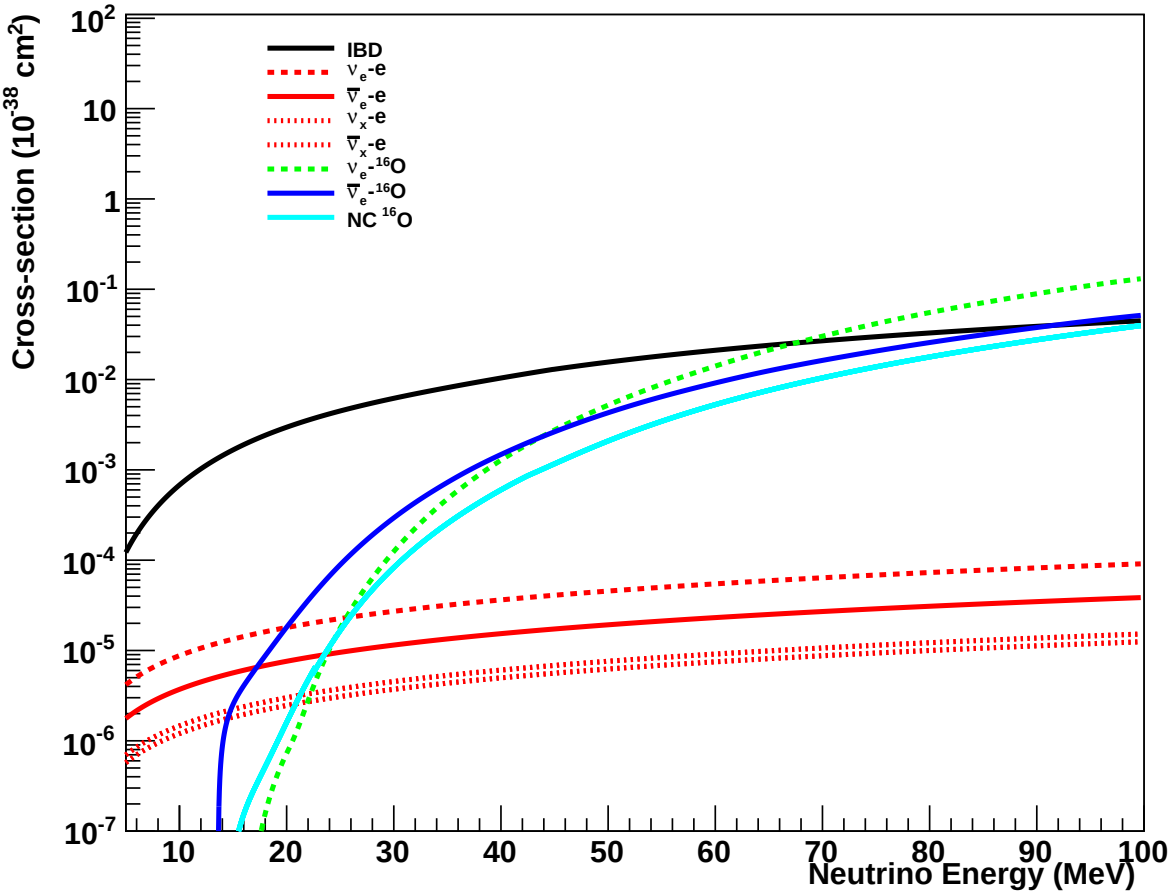

Figure 3.2: The cross sections for the dominant channels in water. In detail, the IBD and neutrino-electron ES are computed from [43] and [29] respectively. The cross sections for Oxygen channels are from [23]. The graph is taken from SNOwGLoBES.

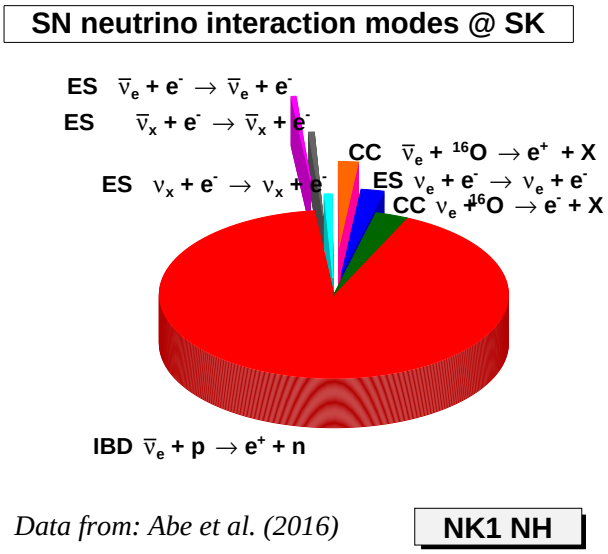

Figure 3.3: Pie chart of the SN neutrino interaction modes at Super-Kamiokande based on the data available on [1] for the Nakazato model in normal hierarchy scenario.

3.4 Photomultiplier tubes

The 20-inch PMT[5] of the ID has bialkali (*Sb-K-Cs*) photocathode sensitive to light in the interval between about 300 and 600 nm. A PMT schematic is illustrated in figure 3.4

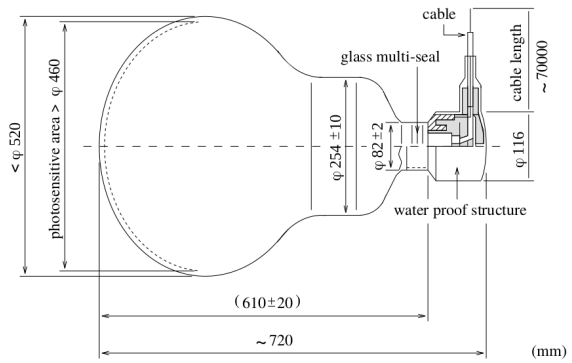

Figure 3.4: Schematic of the 20-inch PMT of the SK ID. Figure from [13]

The quantum efficiency as function of wavelength is displayed in figure 3.5 and it peaks at 360–400 nm with the maximum of $\sim$ 20%. In order to improve the vertex reconstruction quality, the good

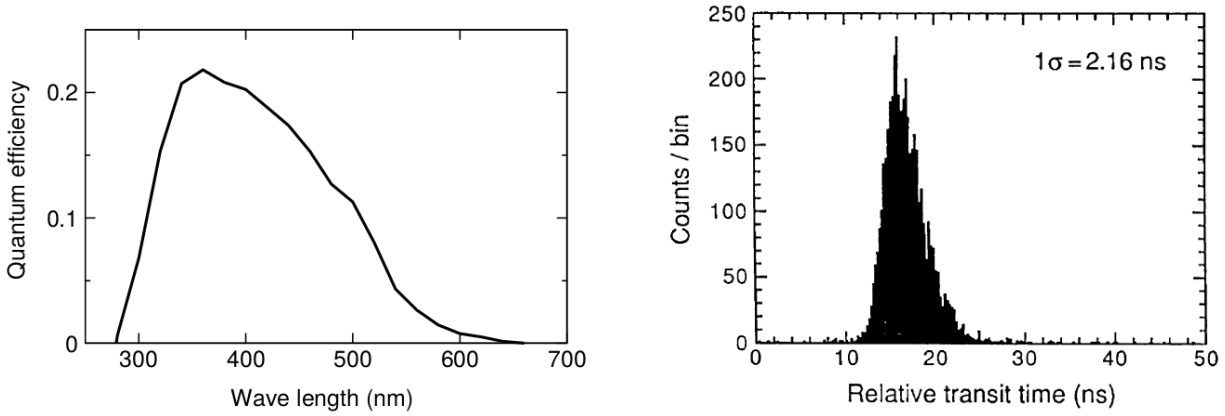

Figure 3.5: (*Left*) Quantum efficiency vs wavelength and (*Right*) transit time spread of the 20-inch PMT (Inner Detector SK). Figures from [13]

timing resolution is required, as we shall see in the next section. As displayed in figure 3.5 , for single photoelectron, the transit time spread is 2.2 ns. Lastly, the mean dark noise rate is about 3 kHz at the 0.25 p.e. threshold operating at SK .

[5]model: *Hamamatsu R3600*

3.5 Low-energy event reconstruction

In the SK system, the energy information is inferred by the response of the PMTs.

The events with less than 1,000 PMT hits, *i.e.* with energy < 100 MeV, are classified as *low energy* (LOWE or LE), in contrast to the so-called *high-energy* (HE) neutrinos. Different techniques have been developed to its analyses. A typical LOWE electron event is displayed in figure 3.6

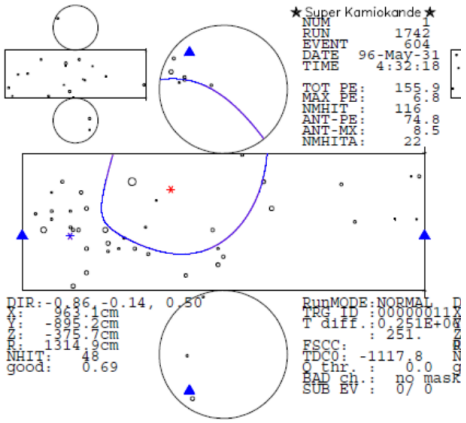

Figure 3.6: Event display of a LOWE electron, detected and reconstructed by the SK framework. Figure from [46]

The LE event reconstruction is based only on the absolute number of PMT fired. This hypothesis is justified by the fact that single p.e. is generated for most of the PMTs triggered in the LE detection.

Since the *charge* response is negligible, only the relative timing distribution of the PMT hits is additionally required to perform the complete *vertex* reconstruction as it shall be described in the next paragraph.

3.5.1 Vertex reconstruction

The LE neutrino interactions in water produce electrons or positrons because the other flavour channels are forbidden due to the energy thresholds. Since the average travelled distance in the SK volume is ≈ 10 cm [6] whereas the vertex resolution is 50 cm, the Cherenkov light is assumed to be emitted by point-like source. This light is collected by the PMTs and the PMT timing is extracted from the time of arrival of the first photoelectron.

These data are the input for one of the available vertex fitters. Currently the vertex reconstruction is performed by BONSAI [41] which has the best resolution.

The BONSAI vertex search is a two-step process summarized as follows:

- search the possible *emission points* through the combination of 4 *good hits*. After sorting PMT hits by time, the so-called *good hits* are extracted filtering via the *causality constraint*[7] that must hold for each pair of the selected hits. The i-th PMT residual time is computed for each candidate vertex $\vec{x}_0$ as

$$\Delta t_i = t_i - t_{TOF}(\vec{x}_0) - t_0 \tag{3.4}$$

  where

[6] the stopping power for the electron(positron) in water is $\sim 2\,\mathrm{MeV/cm}$.

[7] *i.e.* the distance between two PMT hits $d_{ij} = |\vec{x}_i - \vec{x}_j|$ must be greater than the product of the speed of light in water and the difference between the time of arrivals of the farther and the closer PMT with respect to the candidate vertex $\vec{x}_0$

$$(t_i - t_j)\frac{c}{n_{water}} < d_{ij}$$

with $d_{i0} > d_{j0}$.

- t_i is the measured hit time;
- $t_{TOF}(\vec{x}_0)$ is the time of flight from the candidate Cherenkov vertex to the i-th PMT;
- t_0 is the candidate Cherenkov light emission time.

- compute the likelihoods for each candidate vertex $\vec{x}$, defined as

$$\mathcal{L}(\vec{x}, t_0) = \log\left\{\Pi_{i=1}^{N_{hits}} f_{PDF}(\Delta t_i(\vec{x}))\right\} \tag{3.5}$$

where the PDF is empirically derived from the LINAC calibrations.

Lastly the search for the maximum likelihood is carried out iteratively, assuming the PMT dark noise as flat in time, and the related emission point is outputted as the best vertex.

Additionally BONSAI provides the goodness of fit parameter γ defined as

$$\gamma = \frac{\sum_i^{N_{hits}} w_i \exp\left\{-\frac{1}{2}\left(\frac{\Delta t_i}{\sigma_{PMT}}\right)^2\right\}}{\sum_i^{N_{hits}} w_i} \quad \text{with} \quad w_i = \exp\left\{-\frac{1}{2}\left(\frac{\Delta t_i}{\omega}\right)^2\right\} \tag{3.6}$$

with $\sigma_{PMT} = 3\,\text{ns}$ and $\omega = 60\,\text{ns}$. This is exploited as one of the real-time filters in the SN online monitor as it shall be see in section 4.2.

3.5.2 Direction reconstruction

The direction reconstruction in SK is based on the Cherenkov ring pattern. For ultra-relativistic electron ($\beta \sim 1$) the Cherenkov angle is peaked at $\sim 42°$, however additional corrections are needed to take into account multiple scatterings. After finding the candidate vertex, the direction $\vec{d}$ is evaluated via the maximization of the likelihood

$$\mathcal{L}(\vec{d}) = \sum_{i=1}^{N_{20}} \log\left\{f_{dir}(\cos\theta_i^{dir}, E)\right\} \times \frac{\cos\Theta_i}{a(\Theta_i)} \tag{3.7}$$

where :

- N_{20} is the number of hits in the interval $[\Delta t - (20\text{ns}), \Delta\text{t} + (20\text{ns})]$, and $\Delta t \approx 0$ given by equation 3.4;
- θ_i is the angle between the candidate vector $\vec{d}$ and the direction defined by the vertex position $\vec{x}_0$ and the position $\vec{x}_i$ of the *i-th* PMT;
- f_{dir} is the PDF of the hit pattern which depends on energy because the multiple scattering is energy-dependent. This dependency is estimated via SK MC simulations of monoenergetic electrons.
- Θ_i is the angle between Cherenkov photons from the reconstructed vertex and the normal of the *i-th* PMT surface;
- $a(\Theta_i)$ is the *acceptance* of the *i-th* PMT which depends on the incident angle.

After the maximization via grid search, the goodness of the fitness is evaluated through the distribution of Cherenkov photons in the Cherenkov cone. Since the distribution must be uniform in the ideal case , the figure of merit[8]

$$\text{dirKS} = \frac{1}{2\pi}\left[\max\left\{\theta_\text{i} - \frac{2\pi\text{i}}{\text{N}}\right\}_{\text{i=1,...,N}} - \min\left\{\theta_\text{i} - \frac{2\pi\text{i}}{\text{N}}\right\}_{\text{i=1,...,N}}\right]$$

is computed via Kolmogorov-Smirnov test where *max* (and *min*) stands for the maximal (minimal) deviation from the uniform distribution.

[8] a *good* fit is when $dirKS \to 0$, whereas *poor* fit is for $dirKS \to 1$

3.5.3 Energy reconstruction

In the low energy regime the energy reconstruction is mainly based on the number of PMT hits. Since the Cherenkov photon yield is low, the energy is actually proportional to the fired PMTs, however some corrections are needed to take into account the non-linearity of the Cherenkov light production process. In this regard the *effective hit* number is evaluated as

$$N_{eff} = \sum_{i=1}^{N_{50}} \left[(X_i + \epsilon_{tail} - \epsilon^i_{dark}) \times \frac{N_{all}}{N_{working}} \times \frac{R_{cover}}{S(\theta_i, \phi_i)} \times \frac{1}{QE_i(t)} \times \exp\left(\frac{r_i}{\lambda_{eff}}\right) \right]$$

with:

- N_{50} is the number of hits in the interval ± 50 ns centered at residual time $\Delta t \approx 0$;
- X_i is the *occupancy* correction for multiple p.e. in a single PMT based on Poisson statistics hypothesis;
- ϵ_{tail} is the so-called *tail hit* correction which accounts for hits beyond the 50 ns interval;
- ϵ^i_{dark} is the PMT *dark noise* correction evaluated run-by-run and for each PMT;
- $N_{working}$ is the number of operating PMTs and the related factor accounts for the *dead* PMTs on run-by-run basis;
- the factor $\frac{R_{cover}}{S(\theta_i,\phi_i)}$ parametrize the PMT photon coverage;
- QE(t, i) is the quantum efficiency of the *i-th* PMT which critically depends on the gain stability that must be monitor carefully over time;
- r_i is the Cherenkov light distance to reach the *i-th* PMT, and λ_{eff} is the *water transparency* that is controlled by means of laser calibration.

The conversion between the *effective hit* number to the electron energy is provided by the empirical model [27]

$$E = \sum_{i=0}^{4} a_i (N_{eff})^i \qquad \text{if } N_{eff} < 189.8$$

$$E = \sum_{i=0}^{2} a_i (N_{eff})^i \qquad \text{if } N_{eff} > 189.8$$

where the polynomial coefficients are estimated via MC simulations using the calibration data[9] from different techniques that go beyond the scope of this Thesis.

[9] in detail the LINAC calibrations [13] are used to achieve the most accurate absolute energy scale.

Chapter 4

Real-time SN neutrino burst monitor at Super-Kamiokande

4.1 Introduction

Currently, Super-Kamiokande is the only experiment in the globe which might detect the next galactic SN neutrino burst with high-statistics and, simultaneously, localize the astrophysical phenomenon in the sky via the direction of the neutrino-electron scattering channel.

To be ready for this event, the real-time SN neutrino burst monitor, also referred to as *SN watch*, has been working since the 1996, although with different experimental protocols over this period.

The operating scheme (last updated in 2013) is displayed in figure 4.1 and can be summarized as follows:

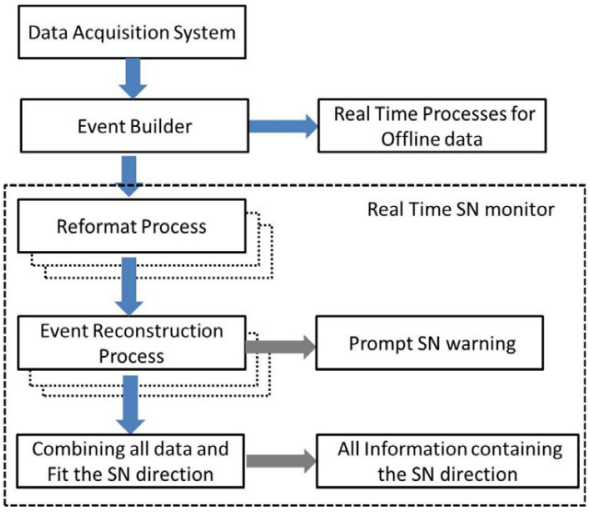

Figure 4.1: Data flow of SN monitor at SK. Figure from [1]

- the *raw* data acquired by DAQ, *i.e.* hit pattern and timing information, are redirected to a dedicated workstation;
- the reformatter convert the raw data into the offline data format;
- the event builder performs an essential analysis to extract relevant information(energy, vertex, direction) of each event in real-time;
- in the aftermath ($\sim$ 2 minutes), the data reduction is carried out selecting, basically, the events with energy greater than 7 MeV and inside the 22.5 kton fiducial volume;

- the search for neutrino burst is performed through dynamic clustering, *i.e.* each event is regarded as starting point of 20-seconds time window, which is opened backward;
- in the case of high-multiplicity SN candidate cluster, the international community, SNEWS included, is promptly alerted, whereas for low-multiplicity SN candidate an internal meeting between SN experts is organized before sending any global warning. The uniformity of the detected vertices must be satisfied by the candidate cluster as well. The current spatial randomness testing relies on the *Principal Component Analysis* (PCA) of the vertex distribution with some additional MC-based constraints as we shall see in section 6.4.2. The search for the most likely SN direction is also performed.

4.2 Data reduction

In the SK system, data are divided into *runs* which have standard duration of 1 day. Each run is split into *subruns* that typically lasts for ≈ 70 seconds. The size of 1-day acquired data is ~ 100 Gb, therefore some online data reduction are needed to reject the dominant background. The selection criteria implemented in the so-called *first reduction*[1] are described as follows.

Fiducial volume In the LE analysis the SK sensitive volume is shrunk to 22.5 kton since most of the radioactive background from surrounding rocks is expected to be produced near the ID walls. In addition the vertices near the internal walls have usually a poor reconstruction quality due to the possible reflections of Cherenkov photons on PMT surfaces. Hence the 2 meters distance cut from the ID walls is applied. It corresponds to accept the event within the radius and height given by

$$\sqrt{x^2 + y^2} := R \leq 14.9\,\mathrm{m}, \qquad |\mathrm{z}| \leq 16.1\,\mathrm{m} \tag{4.1}$$

OD Events with more than 19 hits in the VETO detector are considered as an incoming muon and therefore are discarded.

Total charge If the number of PMT hits is above 1,000 the event is considered as HE and therefore rejected.

Time difference All the events that are within 50μs from the previous LE trigger are regarded as background since they are most likely the decay electron of cosmic muon or the secondary tracks of the cosmic muon itself which passes through SK with rate of $\sim$ 2Hz.

Noise to Signal ratio It is computed as $NSR = \frac{N(Q<0.5\mathrm{p.e.})}{N_{all}}$. Since the noisy PMTs collect lower charge than the real hits, the threshold on this parameter permits a good signal-to-background discrimination. In the SN online monitor NSR must be < 0.4

Energy and Goodness Most of the events below 5 MeV are due to radioactive background. Hence the 7 MeV energy threshold set to the online SN monitor, ensures safely the rejection of this component. Additionally the goodness of the vertex reconstruction is required as well. To this purpose the γ parameter (defined in the equation 3.6) must be > 0.4.

Calibration runs As some calibrations occur (*e.g.* LINAC, Ni, fake SN injection, ...) the related sub-runs are labeled accordingly to recognize them in the offline analyses but are not available in the online monitoring. The duty cycle of the real-time monitor is 97% [1].

[1] there is also a *second reduction* in the SK LOWE analysis but it is not applied in the real-time SN monitor due to the short-latency constraint.

4.3 Expected event rate

The performances of the SK real-time NB monitor have been tested with three SN models before setting the alert system. As reported in [1], the studied models are: the Wilson[45], and the Nakazato[33]. In the latter case the features of the sub-models selected from the open database, are[2] summarized in table 4.1 where t_{revive} is the shock revival time.

Model	M [$M_\odot$]	Metallicity	t_{revive} [ms]
NK1	20	0.02	200
NK2	13	0.004	100

Table 4.1: Selected SN models from the Nakazato database[33] for the full MC simulation of the SN watch response at SK

Additionally the neutrino oscillations, in normal and inverted hierarchies (see appendix 7), have been taken into account based on [12], whereas the collective effects have been neglected.

Assuming the SN source being at 10 kpc, the results of the full MC simulations[3] involving these models are provided in figure 4.2.

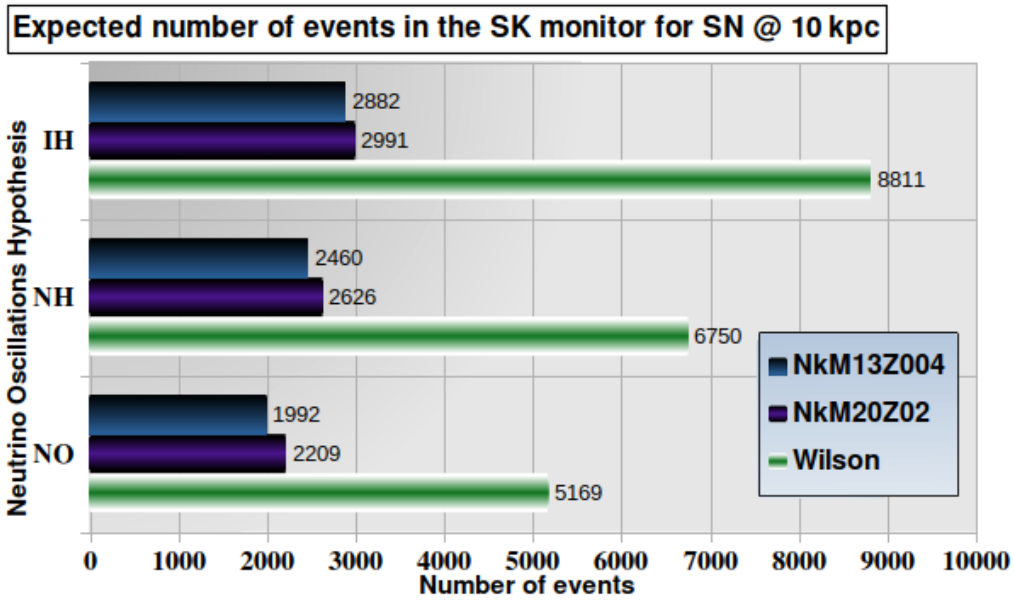

Figure 4.2: The expected event rate in the Super-Kamiokande real-time burst monitor for SN source at 10 kpc distance. The graph is elaborated from the data available on [1].

In general, let i be one of the possible SN neutrino interaction channel in water detector (see section 3.3), the SN *event rate* for this mode is computed as

$$\left.\frac{dN_{det}}{dt}\right|_i = \frac{N_{target}}{4\pi D^2} \int \frac{d^2N_\nu}{dE\,dt}\,\sigma_i(E_\nu)\,\epsilon(E_\nu)dE_\nu \tag{4.2}$$

with

- N_{target} is the number of target nuclei in the active volume of the detector;
- D is the distance of the astrophysical object;
- $\epsilon(E_\nu)$ is the detection efficiency as function of SN neutrino energy;

[2]The rationale behind these choices, consist of the NK1 model has the same progenitor mass of SN1987A, whereas the NK2 has the minimum neutrino flux between all the available models in the database.

[3]the flagship SK reconstruction suite is built on custom GEANT3 routines.

- $\sigma_i(E_\nu)$ is the interaction cross section in water;
- $\frac{d^2N_\nu}{dE\,dt}$ is the number luminosity[4] outputted by the CCSN model.

Thus, the expect number of event for an other distance d can be estimated by scaling via the inverse square law. [5]

4.4 Alert system

The current *SN watch* warning system relies on the MC studies described in the previous section. The detected clusters are selected only on the multiplicity $M_{cluster}$ and on the vertex distribution. The uniformity of the vertex distribution is evaluated by means of the paramater *dimension D* which reaches its maximum (equal to three) for uniform volume-like event, as we shall see technically in section 6.4.2. In detail, the alert hierarchy is based on:

- if $M_{cluster} \geq 60$ and $D = 3$, the *golden* warning is set up. This high-priority bulletin is sent automatically to all the SK SN experts (via phone-calls) that decide, within an hour, whether or not to carry out world-wide alert. The 100% detection efficiency up to Large Magellanic Cloud (50 kpc) is provided by this multiplicity threshold for all the examined SN models;
- if $M_{cluster} \geq 25$ and $D = 3$ the *normal* warning is set up. This alert is filtered by primary experts (within 10 minutes) but it is sent to SNEWS as well. The 100% detection efficiency up to Small Magellanic Cloud (64 kpc) is achieved with this multiplicity requirement under the same hypotheses ;
- if $M_{cluster} \geq 13$ within 10-seconds time window, the *silent* warning is set up. The typical rate of SW is two per day, mainly due to cosmic ray muon-induced spallation background. Lastly, the stored SW are employed as diagnostic tool to monitor the stability of the system.

As suggested by the theoretical papers [10], this set of constraints is very conservative in contrast to other SN monitor belonging to SNEWS[6]

In particular the time structure of the cluster is not considered as reported in the same article. Thus, new investigations in this direction have been carried out in the context of the Thesis, as we shall see in the next chapter.

[4]The number luminosity spectrum is related to the luminosity via the transformation

$$\frac{d^2N_\nu}{dE\,dt} = \frac{dL_\nu}{dE_\nu}\frac{1}{E_\nu}$$

[5]ie $\frac{d^2N_\nu}{dE\,dt} = \left(\frac{10\,\mathrm{kpc}}{d}\right)^2 \left.\frac{d^2N_\nu}{dE\,dt}\right|_{10\mathrm{kpc}}$

[6]However in that paper, the *non-poissonian* background is not taken into account. This, mainly due to spallation events that cannot be discarded in real-time, is the dominant component of SK SN watch and therefore it strongly affects the choice of the alert system. Thus, any attempt to improve the current SN monitor, must deal with it carefully as we shall approach in chapter 6.

Chapter 5

Neutrino burst recognition algorithms

5.1 Introduction

The main objective of this chapter consists of exploiting the differences between the SN neutrino signal and background time profiles in order to lower the minimum number of events required to provide a prompt alert, *i.e.* extending the horizon visible in real-time. To this purpose, the new proposed neutrino burst recognition algorithms shall be studied and the performance enhancements with respect to the standard SNEWS method, shall be quantified.

5.1.1 Event clustering

One of the fundamental aspects for every real-time SN monitor is the definition of the neutrino burst(NB) recognition algorithm. Several search strategies have been implementented and proposed by different large-scale experiments during the years [2] [13] [1][14]. However all these techniques needs the definition of the clustering algorithm before making any signal-to-noise discrimination.

Let w and T be the time window size and the total observation time, three possible online data clustering are displayed in figures 5.1 and are referred to as:

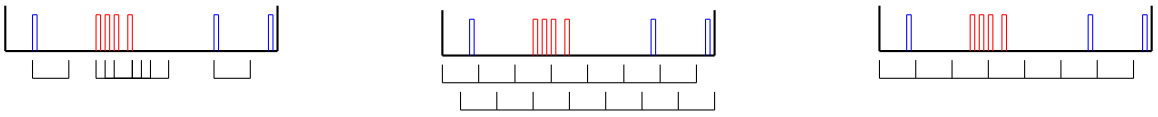

(A) Dynamic (B) Shifted (C)Static

Figure 5.1: Schematic of the *dynamic*, *shifted* and *static* clusterings. The red bars stands for candidate signal, whereas the black ones for the uncorrelated background. In the shifted case the first and second scans are shown.

- *static* clustering: the time interval T is divided into N sliding time-window of size w;
- *shifted* clustering: the scans are performed like the static case, with the second scan, starting from the middle ($w/2$) of the time window of the first one;
- *dynamic* clustering: each event is considered as the starting point of w time window.

The standard size w is set to 20 seconds which is the typical time scale of the SN neutrino emission during the cooling phase [1].

It is worth noting that the *dynamic* clustering preserves all the timing information of the signal within the time window w despite it becomes more and more unfeasible to implement in real-time as the size w and/or the background rate increase. In the *shifted* clustering the substantial bias of

[1] it is a reasonable hypothesis both from theoretical, point of view (section 2.1.6) and in agreement with SN1987A observation (figure 2.4).

the *static* case is partially overcome (still some information is missed) but there is not additional computational latencies. Thus, both cases shall be considered in the following treatment.

5.1.2 Characterization of a cluster in real-time

In general, the SN cluster are characterized by:

- the *multiplicity* (m), *i.e.* the number of events within w time window;
- the time difference Δt between the first and the last event in the cluster.

In SK monitor, for each event of the cluster, the

- energy and goodness (γ) distributions
- vertex position $\vec{x}_i$
- absolute and relative time of arrival t_i

are reconstructed in real-time as well.

5.1.3 Performance testing

In the classification of different NB recognition algorithms, the evaluation of the *false alarm*(FAR) and *false negative* rates are mandatory. These two quantities are also referred to as *type I* and *type II* errors[2].

Background injection

The estimation of the *false alarm rate* has been performed as follows:

- inject the background events, following Poisson distribution with fixed rate r_{bkg} and for the time t_s that must last, at least, the required *false alert time* t_{FAT} (also referred to as *false discovery time*);
- make clustering (*shifted* or *dynamic*) of the toy data;
- apply the neutrino burst recognition algorithm for every cluster and extract the FAR per t_{FAT} according to the number of selected clusters.

In the following analyses, the stationary poissonian backrground hypothesis is considered with constant rate $r_{bkg} = 0.012$ Hz, based on [1].

Signal injection

The probability of localizing a real SN cluster, *i.e.* the complement of type II error[3], depends on how the SN neutrino flux evolves over time. As suggested in [10], a general-purpose time evolution is

$$f_{signal}(t) = e^{-\frac{t}{\tau_{long}}}(1 - e^{-\frac{t}{\tau_{short}}}) \tag{5.1}$$

where τ_{short} is between [10-100] ms, and τ_{long} is greater than 1 s. In fact, this parametrization can interpolate not only the SN1987 spectrum (see 2.4, with $\tau_{long} \approx 1$ s) but it can capture the structure of almost all the low-energy neutrino bursts ejected from similar explosions[10].

Thus the signal injection has been carried out as follows:

- set the signal parameters τ_{short} and τ_{long} ;

[2] the two notations shall be used interchangeably in the next part of the Thesis.

[3] it is worth noting that this type II error is defined in time domain, whereas in the chapter 6 the same kind of error shall be considered in spatial domain.

- fix the signal multiplicity or compute the number of expected events for SN burst at given distance d. In the latter case, assuming one of the models described in section 4.3, compute the expected average multiplicity M according to the inverse square law

$$\bar{M} = M_{10}\left(\frac{10\,\mathrm{kpc}}{d}\right)^2$$

  and extract the desidered multiplicity as $M = Poisson(\bar{M})$;

- generate M-events in the time window $\tilde{w} = (w + \frac{w}{2})$ according to $f_{signal}(t)$ distribution with a random offset $\in [0, \frac{w}{2}]$ to avoid the introduction of a systematic error in the *shifted* case.

5.2 Standard fixed-threshold method

In SNEWS, the standard method[4] to evaluate the statistical significance of candidate cluster (in real-time) is based on the so-called *imitation frequency* [10] [2] [4]. Assuming poissonian background with rate r_{bkg}, the imitation frequency F_{im}, for given cluster with multiplicity m, is defined by

$$\mathrm{F}_{im}(\mathrm{m}, r_{bkg}|w) = N_{windows} \times \sum_{k=m}^{\infty} \frac{(w\, r_{bkg})^k e^{-w\, r_{bkg}}}{k!} \tag{5.2}$$

with $N_{windows}$ the number of time windows with fixed size w in a given *false alert time* (t_{FAT}). The default FAR is set to one fake alarm per century for a stand-alone operating detector in SNEWS.

5.2.1 Main issue

The imitation frequency method performs the signal-to-noise discrimination relying only on the cluster multiplicity. As pointed out in [10], the timing information of the burst is completely neglected.

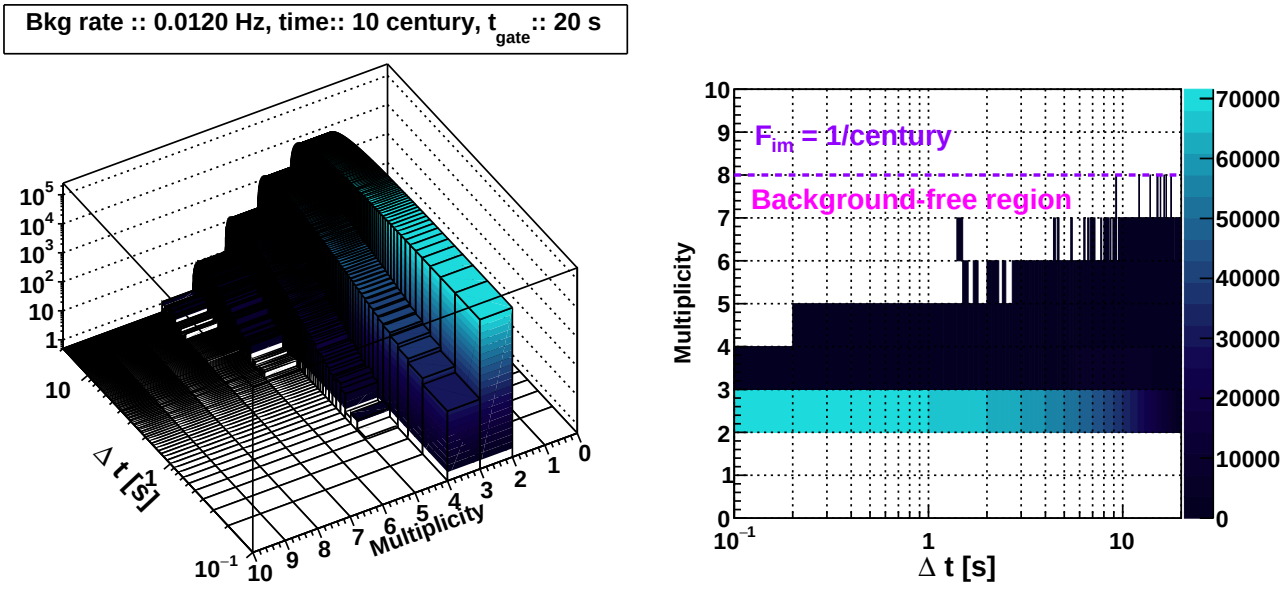

Figure 5.2: Bi-variate distribution with respect to multiplicity and duration of the poissonian background clusters (*shifted* clustering). The dashed violet line represents the standard imitation frequency threshold.

This inefficiency can, therefore, be clearly visualized in the bivariate distribution shown in figure 5.2, where the background events are injected for 10 century with the constant rate r_{bkg} and the

[4] the imitation frequency was also used to set up the multiplicity thresholds in one of the past SK SN watch's protocol, see [13], where the candidate clusters were online searched via time windows of variable size s(0.5,2,10 seconds).

shifted clustering has been carried out. As one can appreciate from the 2d projection of the same chart, the potential low-multiplicity signal clusters, falling into the *background-free* region, are below the fixed threshold defined by the imitation frequency (assuming $t_{FAT} = 1$ century), but they are never explored by background even after 10 times the required false alert time.

5.3 New M-significance method

In order to overcome the standard procedure for real-time NB recognition, the *M-significance* method have been conceived by the author of this Thesis.

Firstly, let us consider the probability of observing m counts in the time t, under the hypothesis of stationary Poisson process with constat rate r. The related probability density function is the convolution of m-exponential distributions with same rate $r = \frac{1}{\lambda}$, *i.e.* the *Gamma distribution*[5]

$$f_m(t) = \frac{t^{m-1}}{\Gamma(m)\,\lambda^m}\, e^{-\frac{t}{\lambda}}$$

thus, the probability is given by the the *Gamma CDF*

$$F_m(t) = \frac{\gamma(m, rt)}{\Gamma(m)} = 1 - \sum_{k=0}^{m-1} \frac{(r\,t)^k\, e^{-r\,t}}{k!}$$

where $\gamma(m, rt)$ is the *incomplete gamma function.*

Hence for each cluster with multiplicity m and duration Δt, the probability

$$\mathbf{F}(m, \Delta t|r) = \sum_{k=m}^{\infty} \frac{(r\,\Delta t)^k\, e^{-r\,\Delta t}}{k!} \tag{5.3}$$

can be computed in real-time. In pratice, it is easier to handle the test-statistic parameter S, named *significance*, and defined by

$$S = -\log_{10} \mathbf{F}(m-1, \Delta t\,|\,r) \tag{5.4}$$

where the first event is assumed as the starting point and therefore the desired probability consists of detecting m-1 events in time Δt.

Ultimately, the new method consists of defining the proper cut on the *significance* (S_{cut}) satisfying the required *false discovery time.* It is worth mentioning that the S test-statistic can fully replace the multiplicity threshold based on the standard imitation frequency.

5.3.1 Decision boundary

The definition of the *decision boundary* for the *significance* relies on the MC simulations of the background. The strategy implemented to find this cut consists of

- inject and cluster the background events as described in 5.1.3 for the time t_s;
- compute the *significance* for each cluster with multiplicity[6] $m \geq m_{ths}$.
- find the best cut S_{cut} integrating the toy *significance* distribution $f(S)$

$$S_{cut} \qquad : \frac{t_s}{t_{FAT}} = \int_{S_{cut}}^{\infty} f(S)\, dS$$

This technique has been tested assuming the same background rate provided in [1], and simulating events for 10^5 years. The results are illustrated in figures 5.3 and 5.4 and summarized in the table 5.1.

[5] also referred to as *Erlang distribution* for integer values.

[6] the standard multiplicity threshold (m_{ths}) is 2. However, if the SN monitor requires an higher minimum number of events to make a cluster, this constraint must be considered in the evaluation of the best significance, which in turn becomes multiplicity-dependent.

Significance	century^{-1}	year^{-1}	month^{-1}	day^{-1}
dynamic $m_{ths} = 2$	8.32	6.20	5.06	3.42
dynamic $m_{ths} = 4$	8.24	6.07	4.87	3.12
shifted $m_{ths} = 2$	8.48	6.36	5.20	3.58
shifted $m_{ths} = 4$	8.38	6.21	5.00	3.17

Table 5.1: Optimal *Significance* decision boundaries based on toy MC simulations in the dynamic and the shifted clustering.

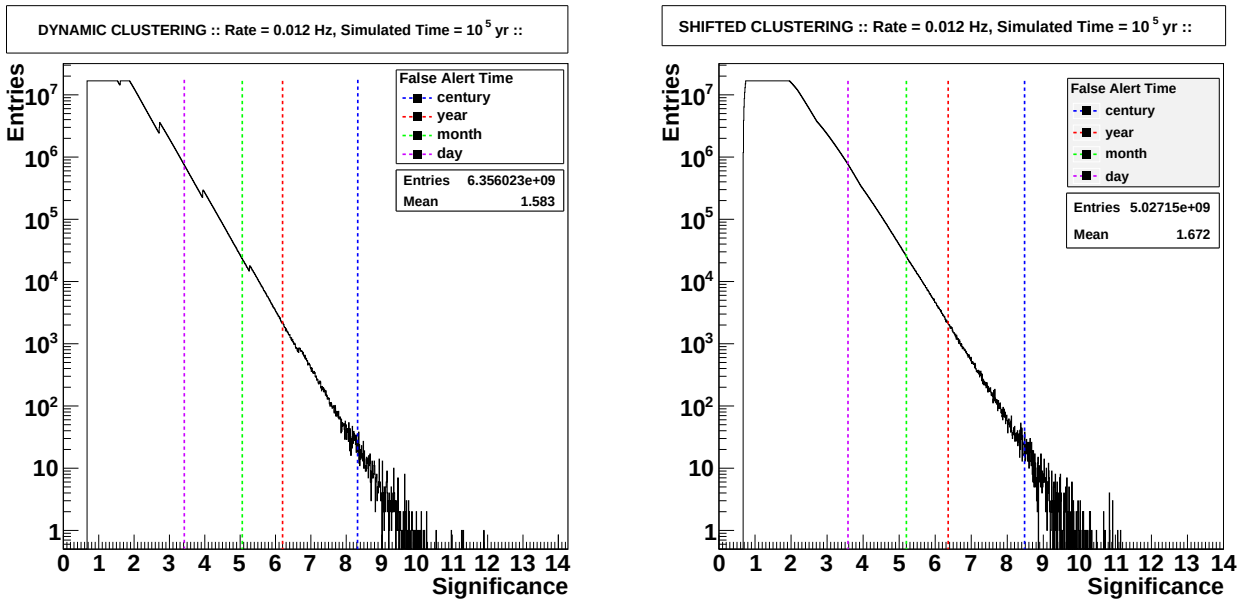

Figure 5.3: Significance distribution for (left) dynamic and (right) shifted clustering with the simulation time of 1,000 centuries. The significance cuts are provided for one century, year, month and day of false discovery time.

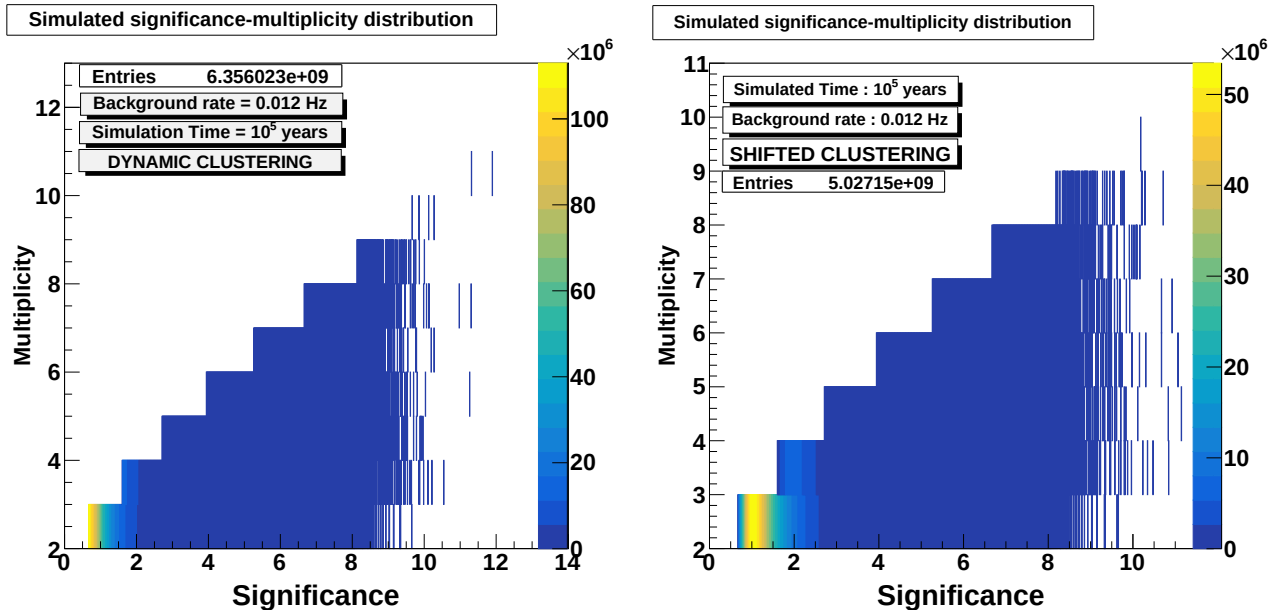

Figure 5.4: Bivariate distribution with respect to significance and multiplicity for (left) dynamic and (right) shifted clustering. The simulation time is set up to 1,000 century with $m_{ths} = 2$.

5.3.2 Robustness analysis

In order to test the robustness of the proposed *significance* estimator, the significance distributions have been computed for several background rates. Thus, fixing the optimal significance S_{cut}, the average number of false alerts per century has been evaluated as function of the poissonian background rate. The results of the performed robustness analysis, for 1,000 century simulation time, are displayed in figure 5.5.

The new proposed method looks stable under reasonable deviations from the assumed background rate r_{bkg}. The stability is crucial for a real application since fluctuations of the background rate, occuring during the data-taking period, shall not cause the proliferation of the false alarms. However further investigations, beyond the scope of the Thesis, are needed to generalize the conclusions, especially in the high-background rate scenario.

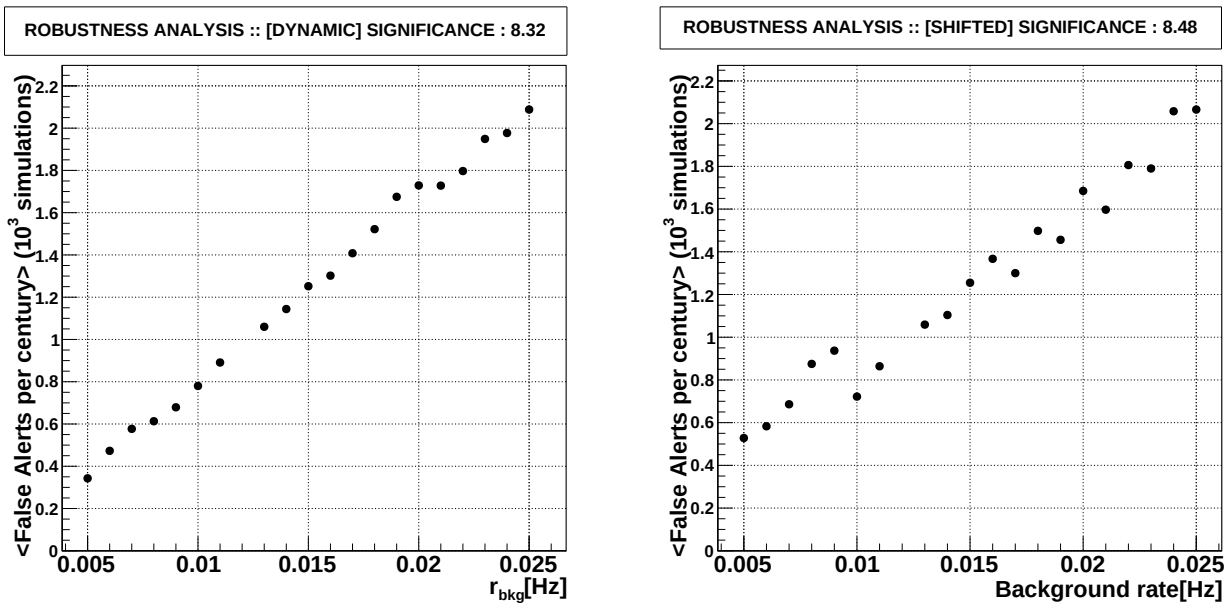

Figure 5.5: Robustness analysis at fixed significance cut S_{cut} and with the simulation time of 1,000 centuries. (Left) Dynamic clustering (Right) Shifted clustering.

5.3.3 Type II error

The next step, required to evaluate the feasibility of the new significance test-statistic, is the study of the *type II* error, *i.e.* the probability of missing a real SN cluster. The *false negatives* rate for the M-significance method, is therefore estimated as follows

- inject the signal as described in 5.1.3 and, in the same time window, the background;
- apply the clustering and select the cluster with the highest significance $S_{max} = max\{S_i\}$;
- iterate N times, with N statistically large enough.

The *signal efficiency* (1-type II error) is provided by the fraction of highest significances above the optimal significance cut S_{cut}. Setting $\tau_{short} = 10ms$ and $\tau_{long} = 1$ s, the achieved results as function of the fixed signal multiplicity, are shown in figure 5.6 according to dynamic and shifted clustering. Assuming the Nakazato model with 13 $M_{\odot}$ and Z=0.02 in the normal hierarchy scenario, the same performances with respect to SN distance, are displayed in the figure 5.7.

In both the dynamic and shifted cases the enhancements in the signal recognition are appreciable with the maximal improvements up to $\approx 80\%$(dynamic) and $\approx 90\%$(shifted) at fixed (6-)multiplicity .

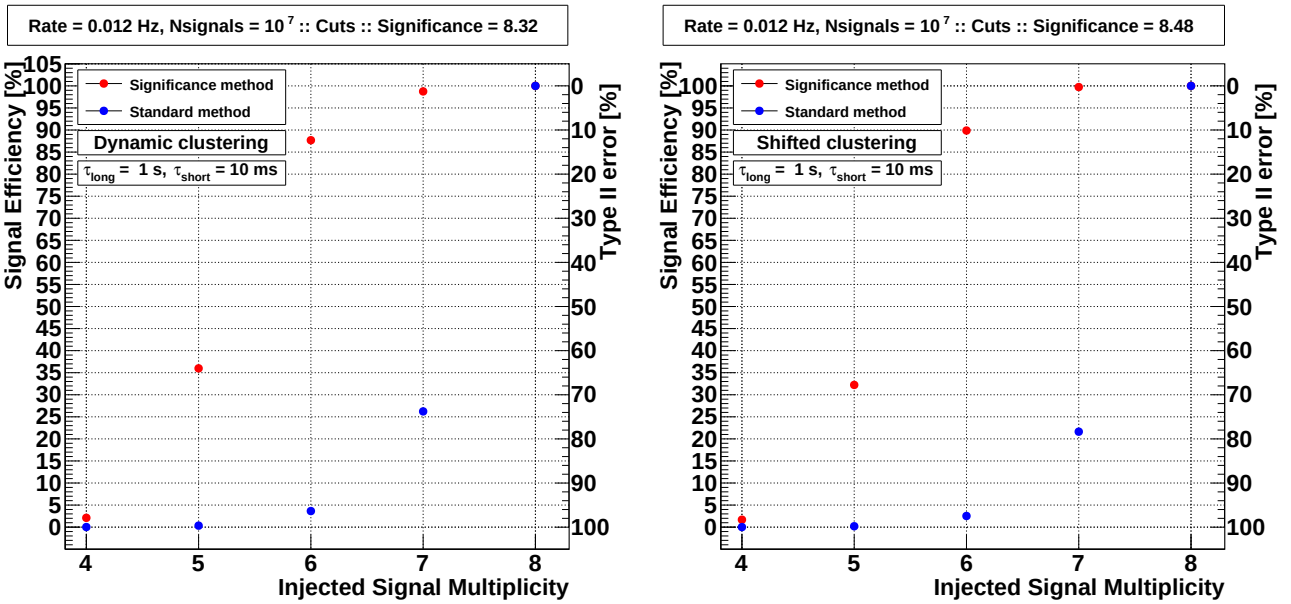

Figure 5.6: Signal efficiency as function of the multiplicity for the significance and the imitation frequency methods. The signal shape is provided by equation 5.1 with $\tau_{short} = 10$ ms and $\tau_{long} = 1$s. (Left) Dynamic clustering. (Right) Shifted clustering.

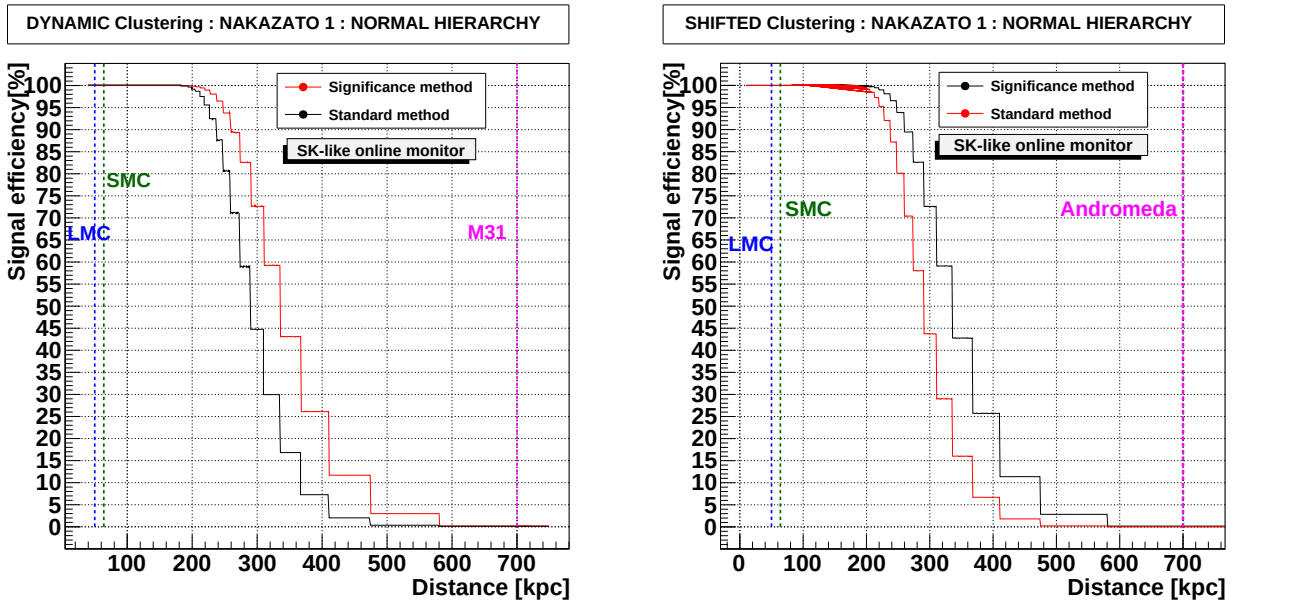

Figure 5.7: Signal efficiency as function of the SN distance (in the NH NK1 model) for the significance and the imitation frequency methods. The signal shape is provided by equation 5.1 with $\tau_{short} = 10$ ms and $\tau_{long} = 1$s. (Left) Dynamic clustering. (Right) Shifted clustering.

5.4 New upsilon method

As an alternative to the *M-significance* method, an additional real-time NB recognition algorithm have been designed and investigated in the scope of the Thesis.

Starting from the probability 5.3, the test-statistic Υ is defined by

$$\Upsilon(m, \Delta t) = N_{windows} \times \mathbf{F}_{m-1}(\Delta t) = N_{windows} \sum_{k=(m-1)}^{\infty} \frac{(r\,\Delta t)^k\, e^{-r\,\Delta t}}{k!} \tag{5.5}$$

where $N_{windows} = \frac{t_{FAT}}{\Delta t}$.

5.4.1 Optimal cut

Likewise the *M-significance* method, the Υ_{cut} is selected such that the cluster rate with $\Upsilon < \Upsilon_{cut}$ is less than one per t_{FAT}.

The Υ distributions with the related optimal cuts are displayed in figure 5.8. The results have been achieved under the same assumptions of the *M-significance* method. In particular the bivariate distribution with respect to Υ and the multiplicity is shown in figure 5.9 and the decision boundaries, valid for[7] $m_{ths} = 2$ and $m_{ths} = 4$, are schematized in the table 5.2.

Υ	century^{-1}	year^{-1}	month^{-1}	day^{-1}
dynamic	4.17	407.4	6.30957×10^3	1.99526×10^5
shifted	3.98	446.68	6.02560×10^3	2.08930×10^5

Table 5.2: Optimal Υ decision boundaries based on toy MC simulations in the dynamic and the shifted clustering.

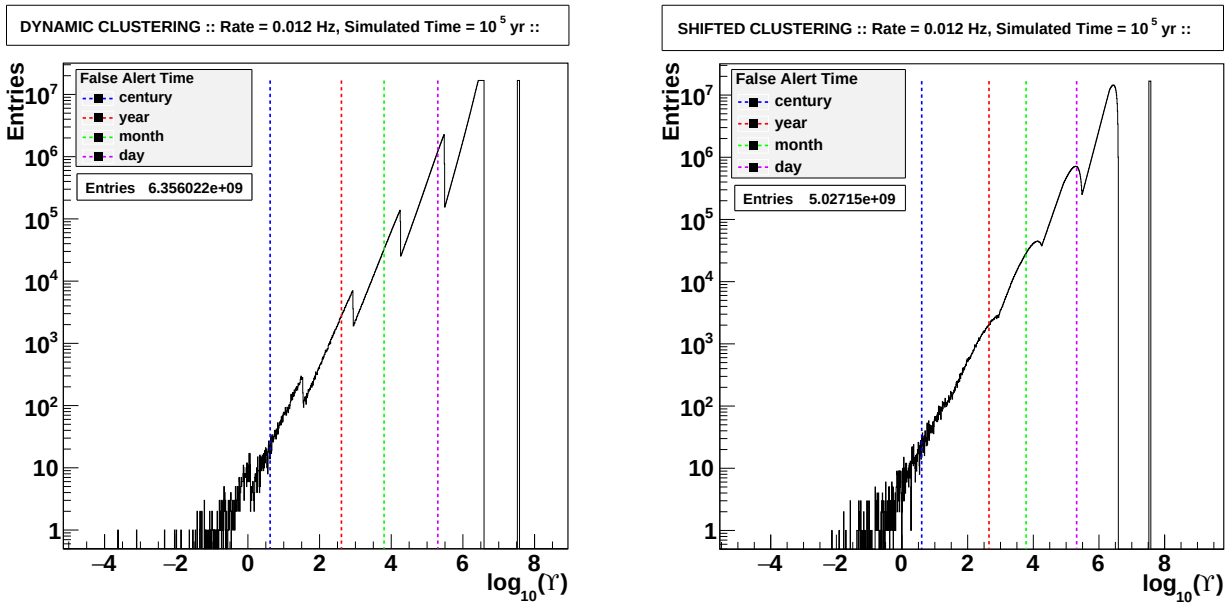

Figure 5.8: Υ distribution for (left) dynamic and (right) shifted clustering with the simulation time of 1,000 centuries. The Υ_{cut} cuts are provided for one century, year, month and day of false discovery time.

5.4.2 Robustness analysis

In analogy with the previous robustness analysis, the outcomes for the Υ parameter injecting the poissonian background for 1,000 centuries, are displayed in figure 5.10. The method is again fairly stable against uncertainties on the background rate.

[7] there are small discrepencies for the Υ_{cut} in the daily *false alert time* but they are neglected in the following treatment .

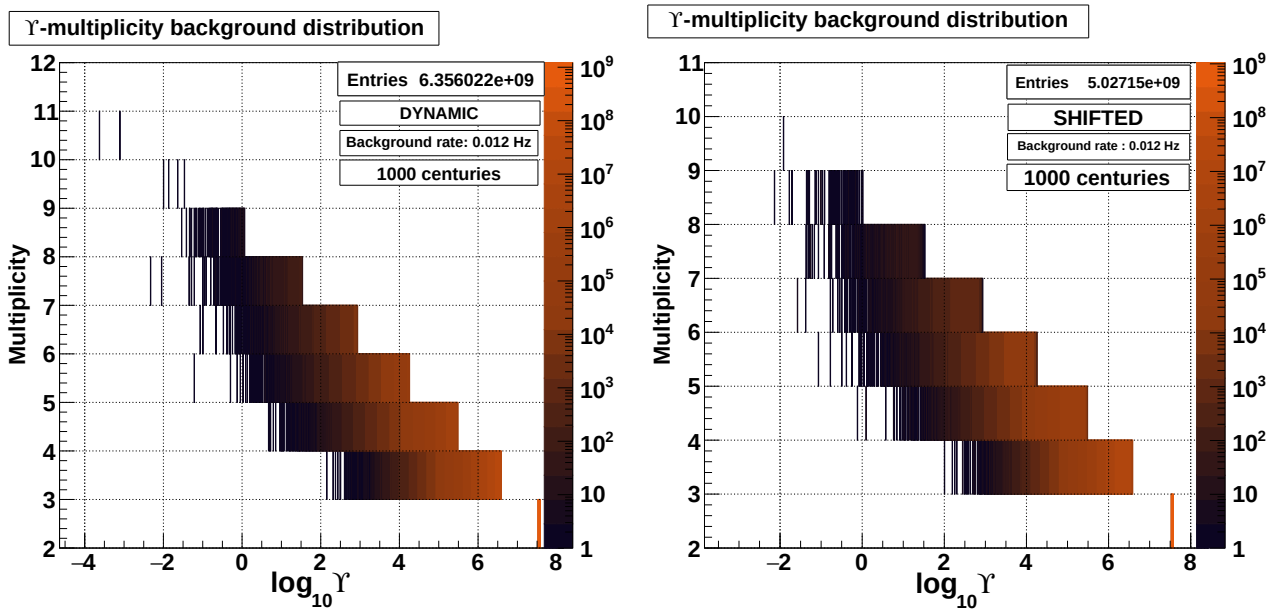

Figure 5.9: Background bivariate distribution with respect to Υ and multiplicity for (left) dynamic and (right) shifted clustering. The simulation time is 1,000 centuries and $m_{ths} = 2$.

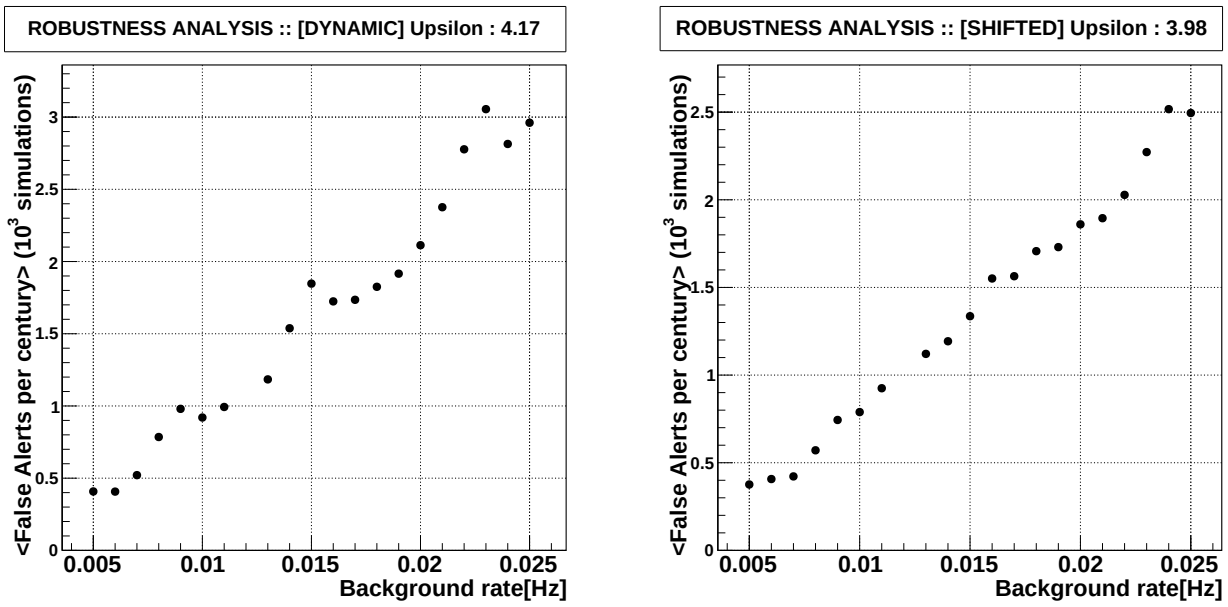

Figure 5.10: Robustness analysis at fixed Υ_{cut} . The simulation time is set up to 1,000 centuries. (Left) Dynamic clustering. (Right) Shifted clustering.

5.4.3 Signal efficiency

The signal efficiencies for the Υ-method as function of multiplicity are illustrated in figure 5.11 under the same hypotheses of section 5.3.3. One can appreciate that the Υ-method performs better at higher multiplicities, viceversa the M-significance is more efficient in the low-multiplicity region.

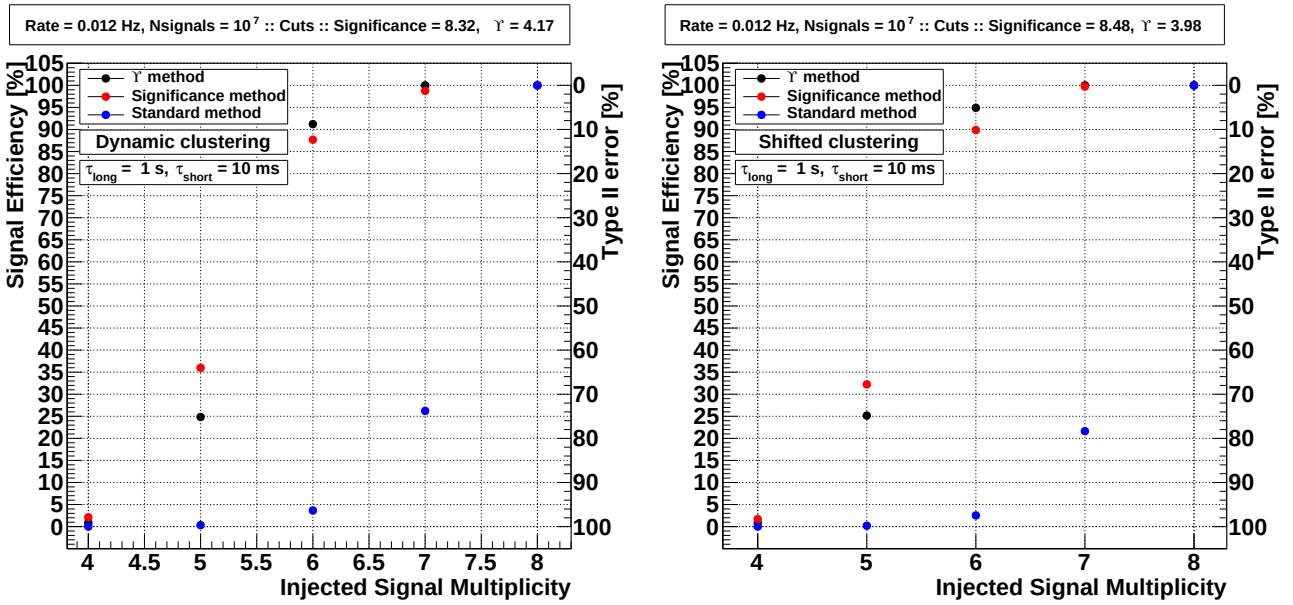

Figure 5.11: Signal efficiency as function of the multiplicity for the significance, the Υ, and the imitation frequency methods. The signal shape is provided by equation 5.1 with $\tau_{short} = 10$ ms and $\tau_{long} = 1$s. (Left) Dynamic clustering. (Right) Shifted clustering.

5.5 Discussion and remarks

In this section the critical analysis of the new developed neutrino burst recognition algorithms is provided.

In view of a potential update of the SK SN monitor[8], the main positive features of the M-significance and Υ methods are:

- *SN model-independent* techniques based not only on the multiplicity but also on the time structure of the searched signal[9];
- easy to implement in real-time providing an appreciable reduction of the required standard SNEWS poissonian multiplicity threshold;
- fairly *robust* against deviations from the assumed (low) poissonian background rate;
- good performances both in the dynamic and shifted clustering;
- *independent* on the nature of the neutrino cluster, *i.e.* it might be used for every transient astrophysical object emitting LE neutrino burst;
- more in general, these statistical methods might be applied to a wide class of real-time selection processes where sliding time windows are involved and a fixed false discovery rate is required in the decision-making.

[8] these considerations might be generalized for the planned real-time SN monitor of the Hyper-Kamionkande detector, and for other large-scale detectors partecipating in the SNEWS network, *e.g.* LVD[2].

[9] however it is worth reminding that the type II error (the complement of the signal efficiency) is affected by the signal shape, which, in turn, it depends on the SN model.

However, the main issues are:

- the signal-to-noise discrimination is performed only on statistical basis which, in turn, is strongly dependent on MC simulations;
- in the low multiplicity scenario for shifted clustering, a good SN cluster might be rejected if the last or the first events are due to uncorrelated background.

Lastly, it is worth mentioning that all the neutrino burst recognition algorithms described in this chapter, relies on the hypothesis of homogeneous poissonian background. Nevertheless, this assumption does not hold for real SN neutrino detectors since there is always non-poissonian noise. This contribution is, especially, critical at SK, where the spallation events due to cosmic-ray muons, are the dominant source of background (~ 2 silent warnings per day, see section 4.4). In order to restore the backbone hypothesis of the NB recognition algorithms, it is, therefore, mandatory performing the online rejection of this component.

To this purpose, the spatial analysis of the reconstructed vertices with the related topological cuts shall be the topic of the next chapter.

Chapter 6

Background topological analysis at Super-Kamiokande

6.1 Introduction

In the second step of the neutrino burst identification, the topological analysis of the candidate cluster is performed. The rationale is the background events which do not follow Poisson distribution are spatially correlated within the SK active volume. In contrast the vertex distribution is supposed to be uniform for SN signal[1].

In the SK experiment, the main sources of non-poissonian background , are:

- cosmic ray muon-induced spallation products;
- PMT flashers;
- environmental radioactivity from the nearby rocks.

The last one is actually rejected imposing an higher energy threshold(7 MeV) and reducing the active volume (22.5 kton) as we have seen in section 4.2.

The spallation is the dominant background component in the 6-18 MeV region [24] instead. This is formed by the β decay products of unstable isotopes orginated, mainly, from the secondaries[2] of CR muon-induced showers. The background spallation isotopes with their half-lives and primary production processes, are summarized in table 6.1.

In addition, about 99 % of these isotopes are generated within 3 meters from the parent muon track with an average lateral dispersion of $\sim$ 1 meters for the broader hadronic showers . Since the tagging of the spallation events using the parent muon track [26] is challenging[3] and even more online due to the additional short-latency constraint[4], the spatial discrimination has been chosen for the real-time monitoring system [1],[13].

The objectives of this part are therefore the topological analysis of the background as well as the review and the development of new techniques in order to test the spatial randomness of the candidate SN clusters. Before entering into the details of the performed spatial analysis, a new event display, designed for this purpose, shall be presented.

6.2 Event display

The event display is a crucial diagnostic tool to reject the non-uniform background cluster at a glance. This is especially important in real-time where fast decisions have to be made in order to furnish world-wide alerts.

[1] this hypothesis is also validated by the full MC simulations as reported in [1].

[2] in the SN neutrino energy region, the most important are neutrons and pions.

[3] the main issue is related to long-lived isotopes which have half-lives greater than the CR muon rate $\mathcal{O}(2)$ Hz at Super-Kamiokande .

[4] it is worth noting that even the sophisticated offline spallation rejection algorithms perform with $\sim$ 90% efficiency [25].

Isotope	$\tau_{1/2}$(s)	Decay mode	Primary process
^{18}N	0.624	β^-	^{18}O(n,p)
^{17}N	4.173	$\beta^- n$	^{18}O(n,n+p)
^{16}N	7.13	$\beta^-\gamma$ (66%), β^- (28%)	(n,p)
^{16}C	0.747	$\beta^- n$	(π^-,n+p)
^{15}C	2.449	$\beta^-\gamma$ (63%), β^- (37%)	(n,2p)
^{14}B	0.0138	$\beta^-\gamma$	(n,3p)
^{13}O	0.0086	β^+	(μ^-,p+2n+μ^-+π^-)
^{13}B	0.0174	β^-	(π^-,2p+n)
^{12}N	0.0110	β^+	(π^+,2p+2n)
^{12}B	0.0202	β^-	(n,α+p)
^{12}Be	0.0236	β^-	(π^-,α+p+n)
^{11}Be	13.8	β^- (55%), $\beta^-\gamma$ (31%)	(n,α+2p)
^{11}Li	0.0085	$\beta^- n$	(π^+,5p+π^++π^0)
^{9}C	0.127	β^+	(n,α+4n)
^{9}Li	0.178	$\beta^- n$ (51%), β^- (49%)	(π^-,α+2p+n)
^{8}B	0.77	β^+	(π^+,α+2p+2n)
^{8}Li	0.838	β^-	(π^-,α+^{2}H+p+n)
^{8}He	0.119	$\beta^-\gamma$ (84%), $\beta^- n$ (16%)	(π^-,^{3}H+4p+n)

Table 6.1: Spallation isotopes at SK. Table adapted from [24]

The current system shows the reconstructed vertices by means of two projections in the *xy*-plane and *zr*-plane[5] of the SK cylindrical volume. In addition the *energy* and the *goodness* distributions as function of the relative time are provided as well.

However the visualization of the spatial distribution is often not straightforward and, therefore, the development of 3D-event display have been carried out by the author of the Thesis based on `ROOT` libraries. An example of silent warning cluster is illustrated[6] in figure 6.1.

Furthermore a new 2D display has been designed. This is built on two complementary polar graphs: in one the standard *xy*-plane projection is shown in polar coordinates (r, θ), whereas in the other the (z, θ) projection is provided. The main advantage of this representation is in the case of high-multiplicity clusters where the vertices can be identified by the angle θ without additional labels. The uniformity of the vertex distribution can be also tested visually[7]. An example of 10-multiplicity signal and background clusters, is illustrated in figure 6.2.

[5] where r is the radius of SK volume and z is the height.

[6] the color palette of the vertices in the 2D projections is, automatically, built on the relative time of arrival of the events.

[7] in the *xy*-plane the uniform distribution of the vertex within the circle is required, whereas in the z-polar graph, the distribution of the *radii* must be uniform.

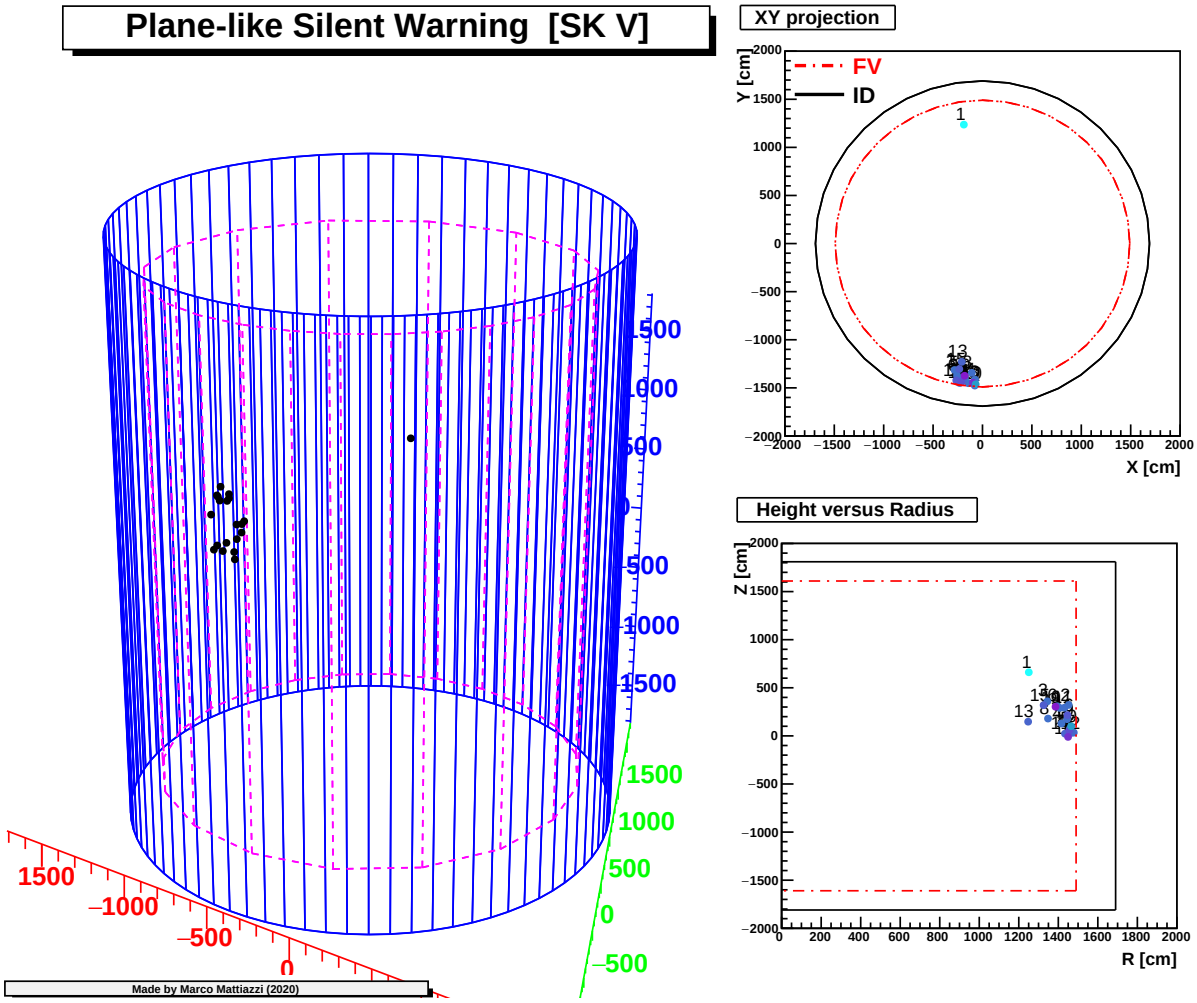

Figure 6.1: Plane-like silent warning detected in the SK V phase

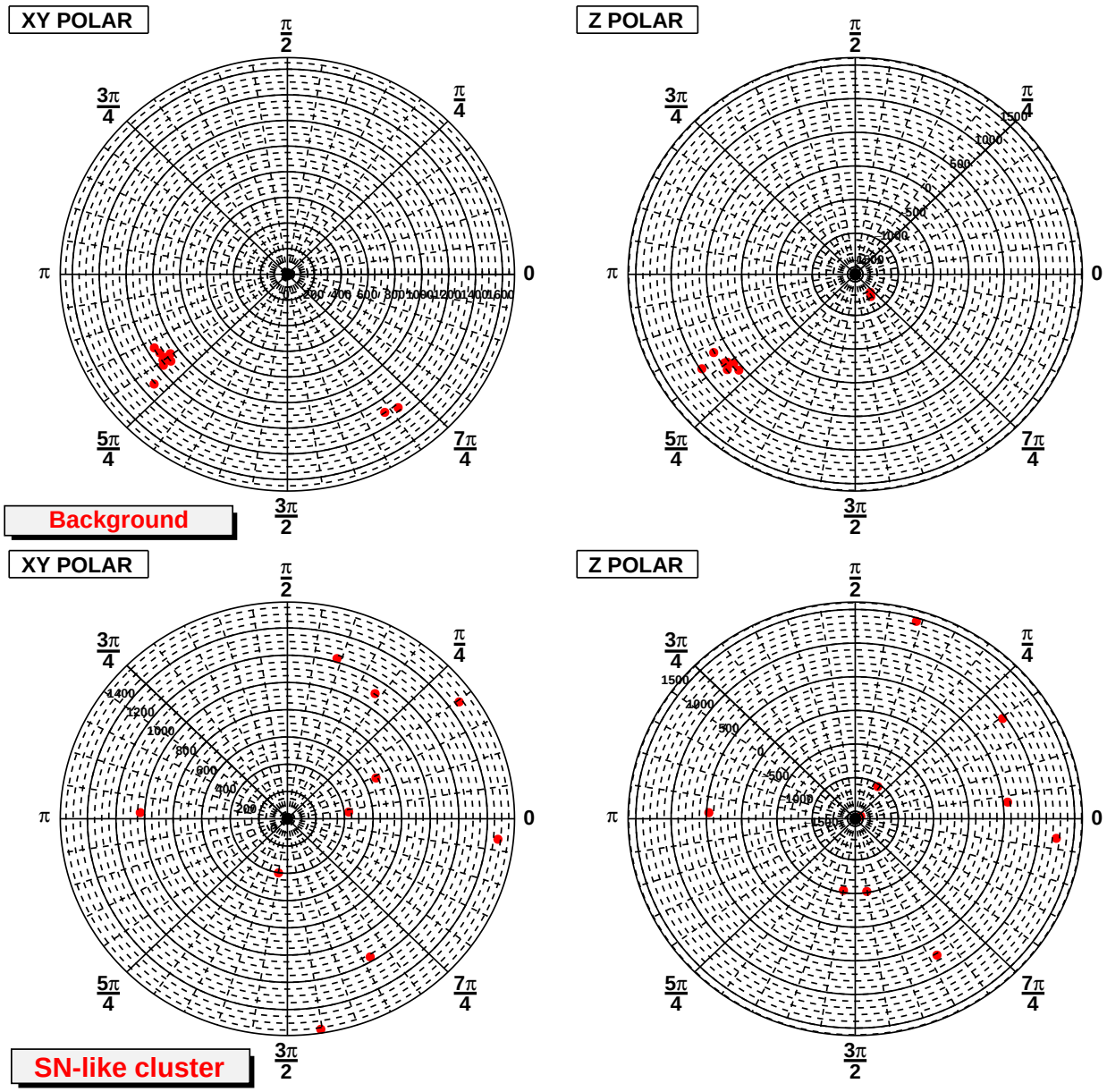

Figure 6.2: (Top) Silent warning-like and (Bottom) SN-like vertex distributions for 10-multiplicity clusters in the new 2D event display.

6.3 Spatial simulation of a cluster

As we have seen in secton 4.4, the non-poissonian background clusters with multiplicity > 12 are saved as *silent warnings*(SW) in the SK online system. Before diving into the spatial discrimination techniques, the topology of these clusters have to be investigated in order to optimize the selection strategy.

Relying on the considerations of section 6.1, the expected SW vertex distribution is

- concentrated around the point-like source for environmental background;
- placed along a cylinder with the maximum diameter $\lesssim 3$ m for spallation events due to their shower origins.

These two cases are actually detected by SK experiment, as illustrated in figures 6.3 and 6.4. Hence, it is fairly straightforward, from the pure topological point of view, to simulate a vertex distribution that looks like this point- and line-like clusters as it shall be described in the next paragraphs.

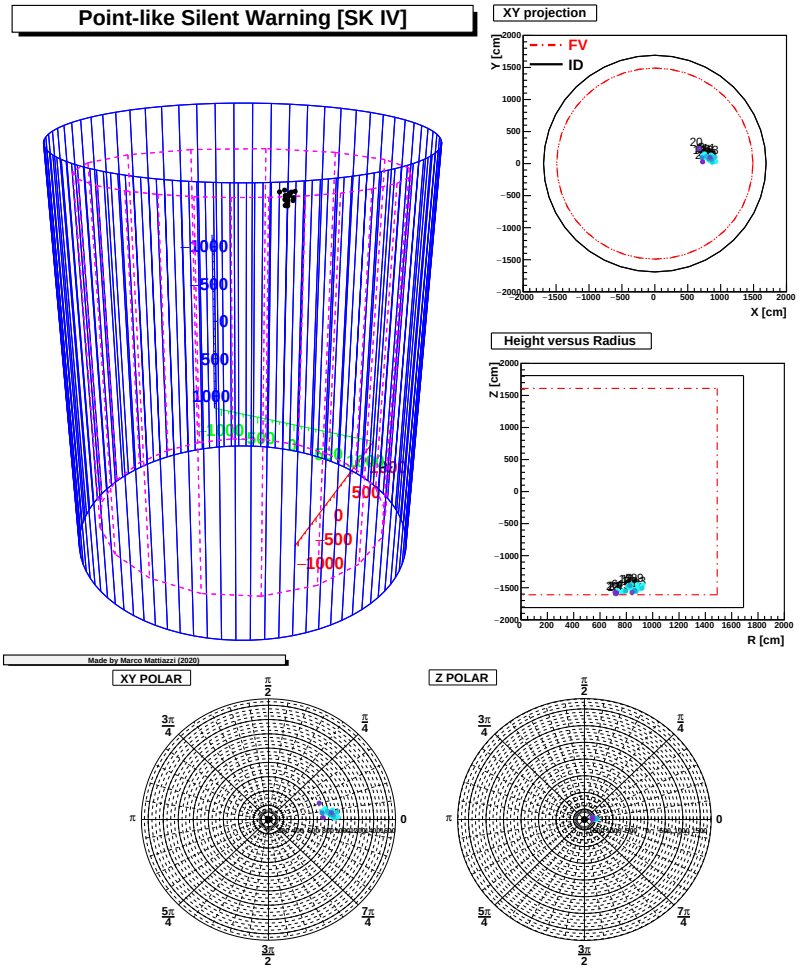

Figure 6.3: Point-like silent warning detected in the SK IV phase

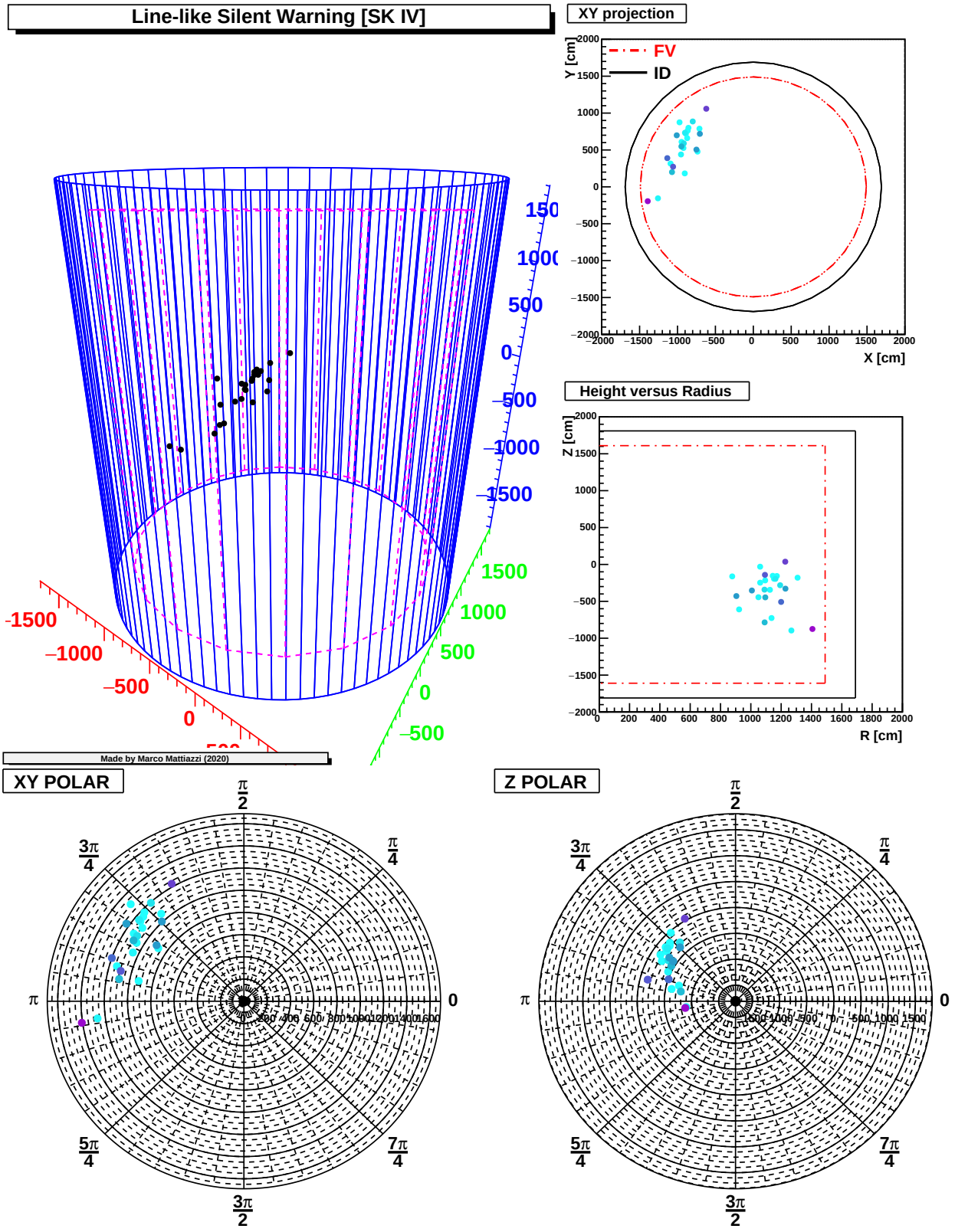

Figure 6.4: Line-like silent warning detected in the SK IV phase

6.3.1 Volume-like source

Before dealing with the possible background spatial distributions, the topology of SN-like cluster is described. As we have mentioned such vertex distribution is supposed to be uniform inside the SK fiducial volume. Thus, the signal has been simulated as *volume-like* source, sampling uniformly in a cylinder [8] with radius r and height h given by the fiducial volume features described in section 4.2. An example of SN-like cluster with multiplicity is depicted in figure 6.5.

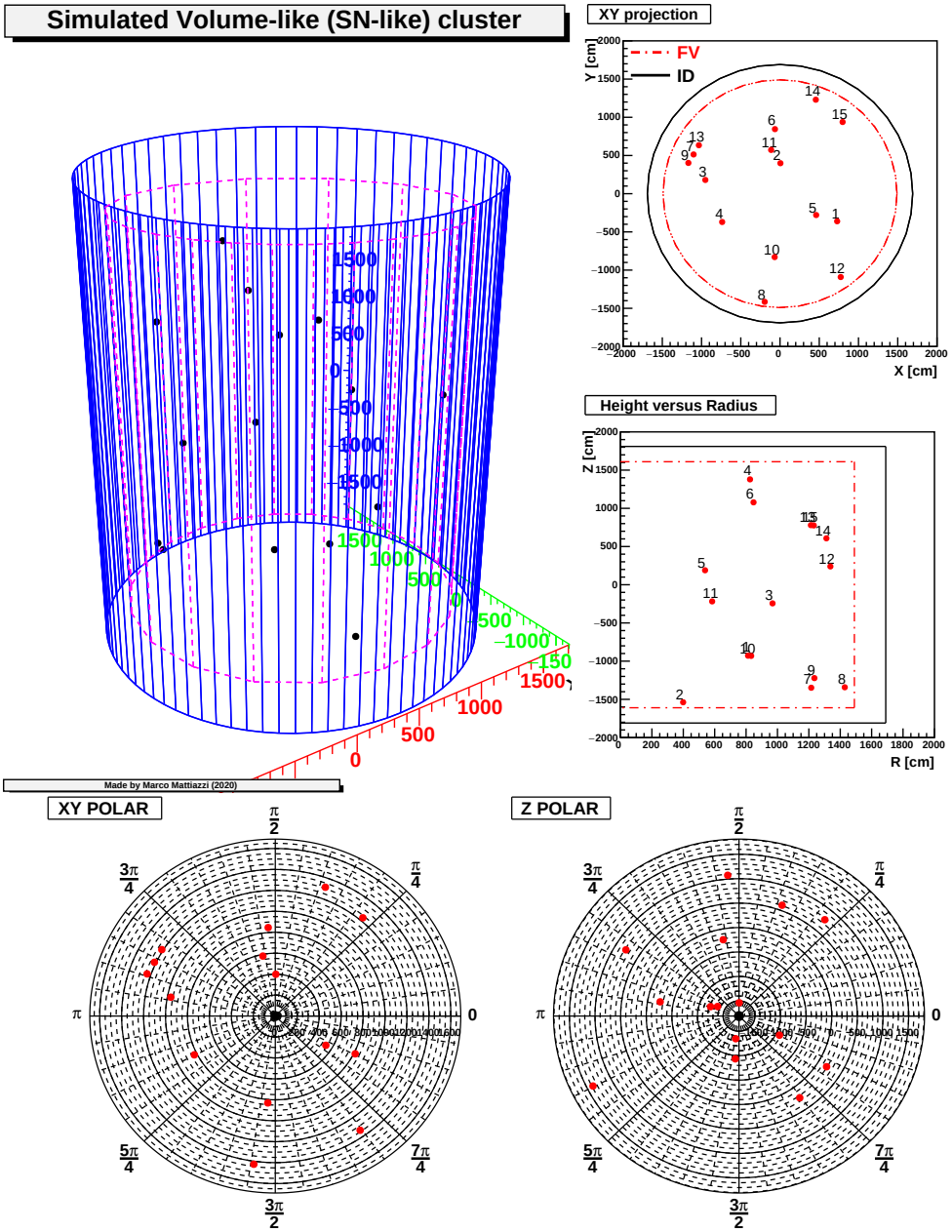

Figure 6.5: Toy volume-like 15-multiplicity cluster.

[8] let u be a uniform random number $u \in \mathcal{U}(0,1)$. A random point inside a cylinder with radius r and height h is basically achieved sampling uniformly on the disk of radius r and on the height, *i.e.*

$$R = r\sqrt{u}$$
$$\theta = 2\pi u$$
$$z = h\,u$$

6.3.2 Point-like source

The clusters from point-like source have been simulated as follows

- set the origin $\vec{x}_0$ as a random point within the SK fiducial volume;
- fix the displacement radius[9] r^P_{disp};
- generate the subsequent M-1 points uniformly inside the sphere centered in $\vec{x}_0$ and with radius r^P_{disp}.

6.3.3 Line-like source

The cluster produced via muon-induced spallation, has been simulated according to the following steps:

- generate the random direction[10] $\vec{v}$ and set the random origin $P_0 = \vec{x}_0$ within SK FV;
- compute the intersection points I_1 and I_2 with the cylinder using the parametric equation of the line
$$\vec{x} = \vec{x}_0 + t\vec{v} \tag{6.1}$$
- sample u uniformly between 0 and d with $d = ||\overrightarrow{I_1 I_2}||$;
- find the point P_i by means of $t^* = u - b_{down}$ with $b_{down} = ||\overrightarrow{I_1 P_0}||$;
- set the displacement radius r^L_{disp};
- shift the point P_i generating a random point inside the sphere with radius r^{LINE}_{disp} and centered on P_i itself.
- iterate the procedure from the u sampling for all the M-1 points P_i.

A schematic of the implemented line-like source generator is illustrated in figure 6.6.

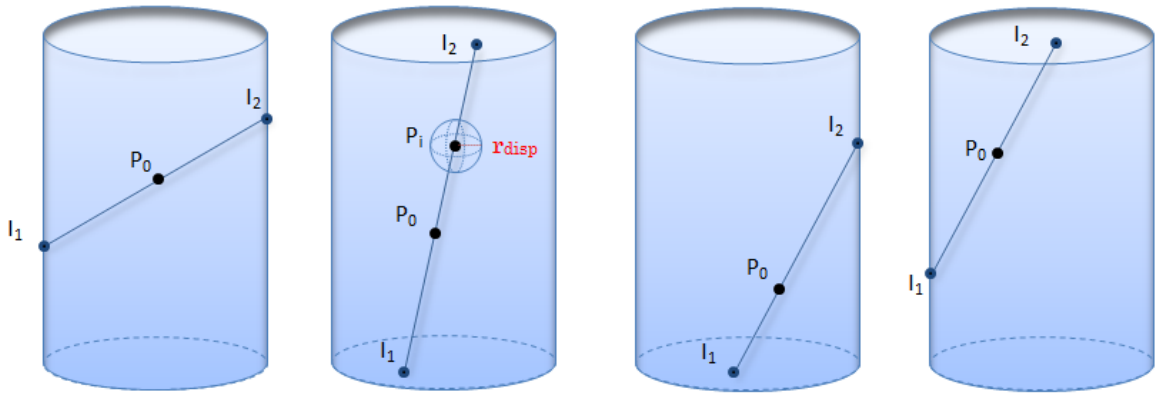

Figure 6.6: Schematic of the line-like source generator

An example of the 15-multiplicity cluster with $r^L_{displacement} = 250$cm, generated by the described routine, is shown in figure 6.7.

[9] in the following MC simulations $r^P_{disp} = 250$ cm is assumed which is greater than the typical maximal dispersion of a real point-like source .

[10] the method `Sphere` from the `TRandom ROOT` class has been used.

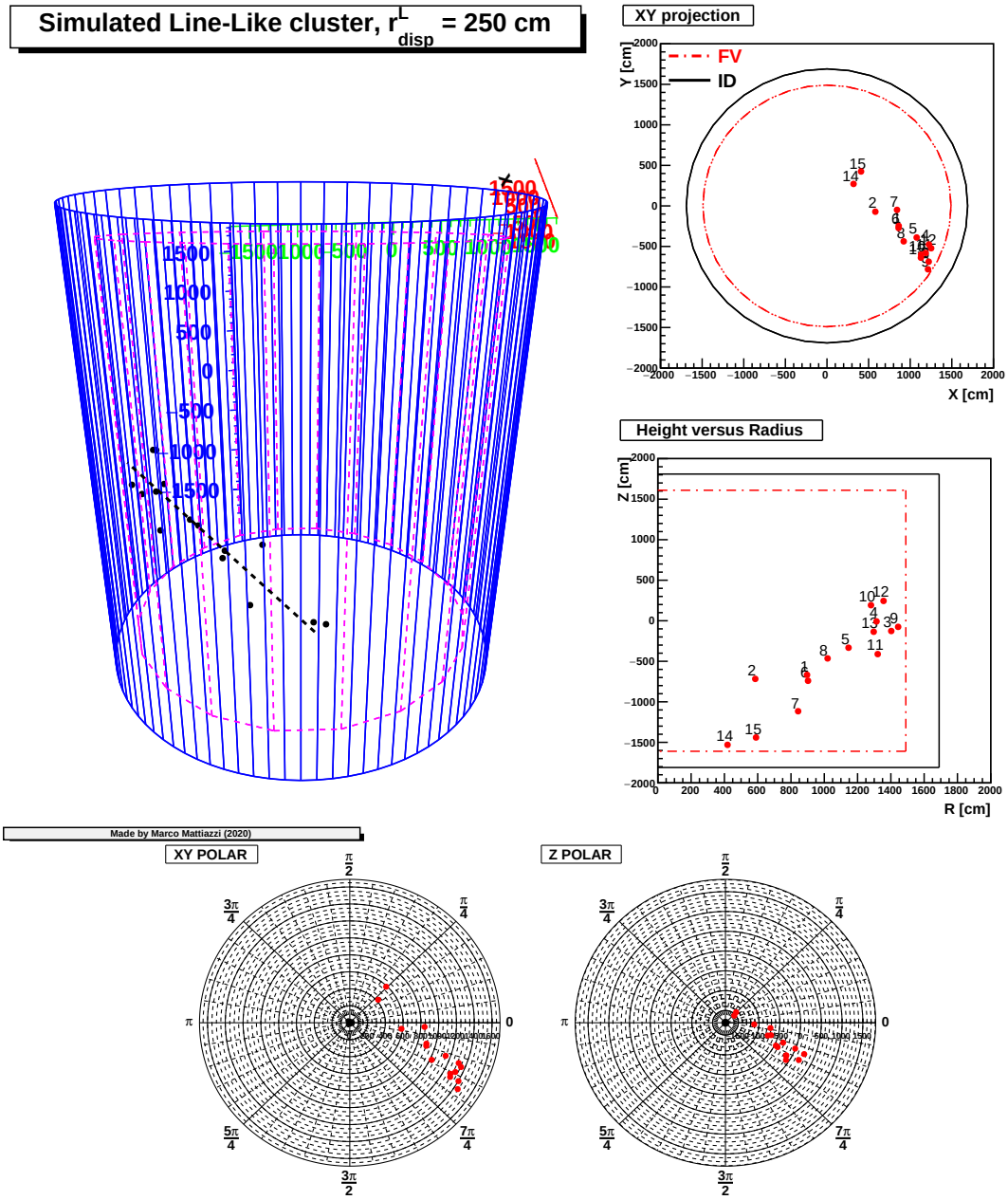

Figure 6.7: Toy line-like 15-multiplicity cluster generated via the custom routines.

6.3.4 Plane-like source

The SW cluster displayed in figure 6.1 is more critical because one uncorrelated hit is present along with the spallation events. The standard procedure to reject this kind of clusters (where there should be more uncorraleted hits) relies on the plane distribution approximation, as reported in [1]. Thus, the simulations of the clusters from plane-like source have been performed in agreement with the following procedure:

- set the origin $\vec{x}_0$ as in the previous cases;
- generate two random directions $\vec{w}$ and $\vec{v}$;
- define the normal to the plane as $\vec{n} = \vec{w} \times \vec{v}$
- sample uniformly in the intersection between the plane and the SK cylinder;
- set the displacement radius and shift the generated points with the same procedure of the line-like case;

An example of simulated plane-like cluster is displayed in figure 6.8.

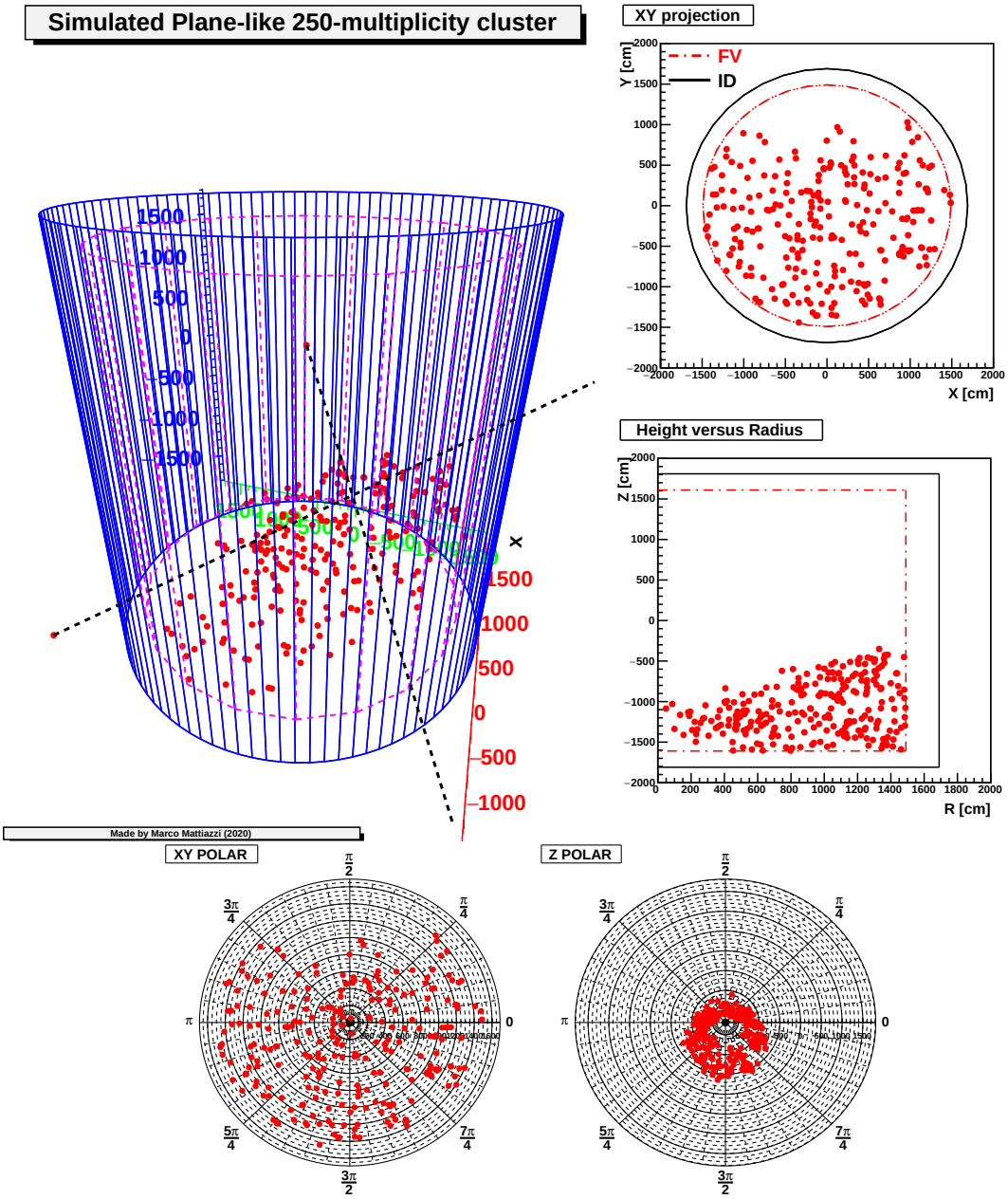

Figure 6.8: Toy plane-like 250-multiplicity cluster generated via the custom macros based on ROOT libraries.

6.4 Topological discrimination techniques

The new neutrino burst recognition algorithms, proposed in chapter 5, enable us to lower the current multiplicity thresholds of the real-time SN monitors. However a careful analysis of the topological cuts is required in order to not vanish the achieved improvements in such low-multiplicity region.

In this regard the old and the current SK spatial discrimination techniques shall be reviewed. In the last part of the section a new technique shall be proposed with the main focus on the very-low multiplicity regime (≤ 13 events per cluster).

Before entering into the details of these methods, the notation used is $X = \{x_i, y_i, z_i\}_{i=1,\dots,M}$ for the set of recostructed vertices and M for the cluster multiplicity.

6.4.1 Average spatial distance

The first method implemented in the SK *SN watch* was based on the average spatial distance between the vertices of the cluster [19] [13]. The spatial uniformity was therefore tested by means of the parameter[11]

$$R_{mean} = \frac{\sum_{i=1}^{M} \sum_{j=i+1}^{M} |\vec{x}_i - \vec{x}_j|}{C_2^M} \tag{6.2}$$

computed for each SN candidate cluster. The decision boundary was set comparing the R_{mean} distribution between *volume-like* and spallation clusters.

The main issue of this method is the high multiplicity required[12] in order to perform the selection without ambiguities and with reasonable signal efficiencies. A toy example is illustrated in figure 6.9 where the 7-multiplicity clusters are injected according to random point-,line[13]-,plane-, and volume-like sources, respectively.

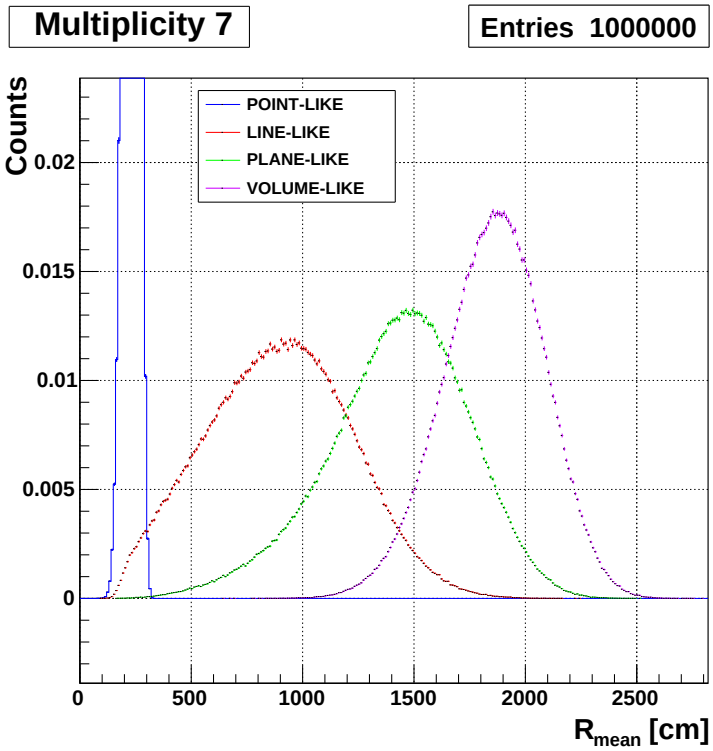

Figure 6.9: Toy example of the R_{mean} distributions computed for 7-multiplicity clusters injected according to point-,line-,plane-, and volume-like sources.

[11] where $C_2^M = \binom{M}{2}$.

[12] in [13] the R_{mean} parameter is computed only for clusters with multiplicity greater than 16.

[13] it is worth pointing out that no limitations are set to the maximum longitudinal size of the line-like source.

6.4.2 Principal component analysis

The current method to discriminate the background clusters, is based on the *Principal Component Analysis* (PCA) of the vertex distribution. The idea behind PCA consists of discarding the redundant degree of freedoms (*dimensional reduction*) of the set X, after the proper change of basis. This is carried out rejecting the dimensions (*components*) where the variance of the data is very small compared to the others[40].

The standard PCA for a general set X with 3 variables and M entries, is performed as follows:

- center the data-set $Y = X - \bar{X}$, with $\bar{X} = \frac{1}{M}\sum_{i=1}^{M} \vec{x}_i$;
- compute the *covariance matrix* $C = \frac{1}{M} YY^T$;
- find the *eigenvalues* $\vec{\lambda} = \{\lambda_1, \lambda_2, \lambda_3\}$ of C where $\lambda_1 > \lambda_2 > \lambda_3$.
- estimate the relavant dimension based on the relative strengths of the eigenvalues. For example, if the ratio

$$R_\lambda = \frac{\lambda_1 + \lambda_2}{\lambda_1 + \lambda_2 + \lambda_3} \tag{6.3}$$

  is close to 1 than the dimension associate with the eigenvalue λ_3 can be neglected with minimal losses.

A toy example of the discrimination power of this technique is illustrated in figure 6.10 where the R_{mean} and the R_λ are computed for 100,000 simulated clusters according to point-,line-,plane-, and volume-like sources.

This procedure is, actually, exploited by the *SN watch* spatial algorithm where some additional stringent MC-based thresholds are made in order to determine the final dimension of the candidate cluster [1]. It is worth mentioning that even in this simplified example the necessity of further decision boundaries beyond the standard PCA technique, is clear. In fact the point-like and volume-like sources have the same eigen-ratio R_λ distributions but they can be discriminated quite easily taking into account the average distance between the vertices.

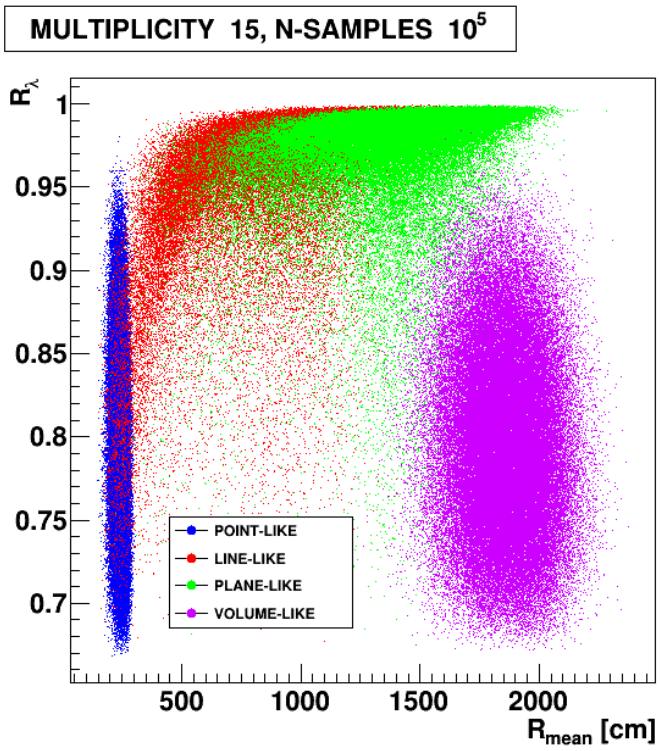

Figure 6.10: Simplified example of the current dimensional discriminator in the real-time SK SN monitor based on PCA of the vertex distribution.

Despite the improved performances, the main issues are

- the PCA is sensitive to outliers, therefore compound background clusters can pass more easily the dimensional fit;
- the stringent thresholds imposed to safely remove the non-poissonian background, dramatically reduce the SN detection efficiency at low multiplicity.

The high selectivity of the dimensional filter is illustrated in figure 6.11 where $\sim 10^7$ volume-like clusters (for every multiplicity) have been injected within the SK FV volume and, after performing the current SK dimensional fit, the fraction of clusters with dimension less than three (false negatives) have been counted.

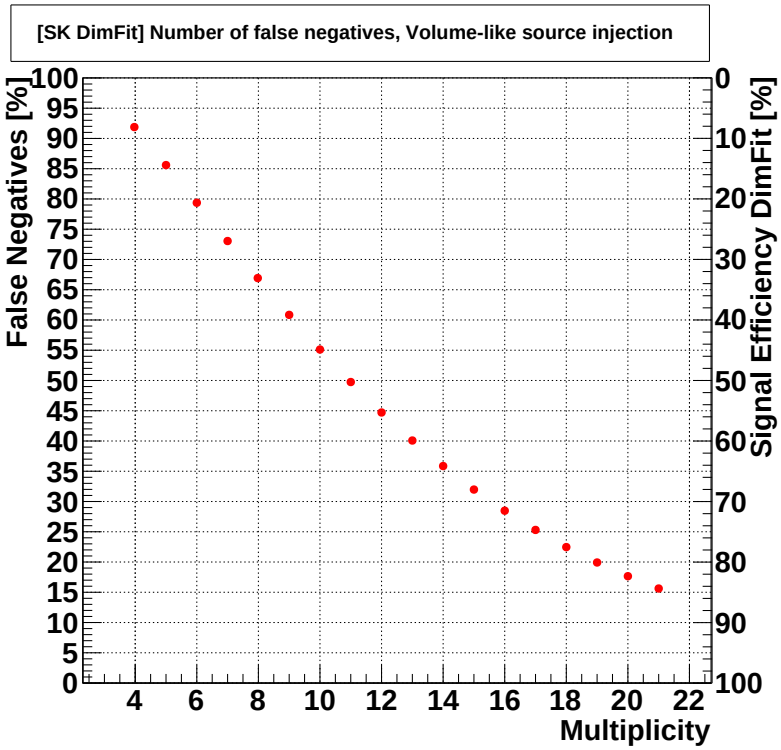

Figure 6.11: Type II error of the current topological cut applied in the SK SN monitor as function of multiplicity. The signal efficiency is computed injecting a sample of $\sim 10^7$ volume-like clusters inside the SK fiducial volume, and, after applying the current SK PCA-based fit, counting the fraction of them with dimension equal to three.

6.4.3 Average nearest neighbor distance

In order to enhance the sensitivity in the very low-multiplicity region, some preliminary studies have been performed relying on the average nearest neighbor (ANN) analysis of the vertices. The key parameter is the ANN distance, defined by

$$W^{(1)}_{NND}(M) = \frac{\sum_{i=1}^{M} \underset{i \neq j}{min}\{|\vec{x}_i - \vec{x}_j|\}_{j=1,\ldots,M}}{M} \tag{6.4}$$

and computed for each cluster. For a complete random spatial pattern, the ANN classifier is supposed to be larger than in the case of spatially-correlated sources.

The proposed method consists in comparing the ANN distance distributions of volume-like(signal) and line-like(background) sources, assuming a displacement greater or equal than the typical lateral development of the CR-muon showers. Thus, the decision boundary $W^{CUT}_{NND}(M)$ is set as the maximum value of the background distribution and the signal efficiency is computed as the fraction of events

that lies above this cut in the SN-like distribution. The MC studies have been performed with the displacement radii r^L_{disp} of 200 and 500 cm. In the latter case, the achieved volume-like and the line-like distributions,up to multiplicity 10, are displayed in figure 6.14. The signal efficiencies are shown in figure 6.12.

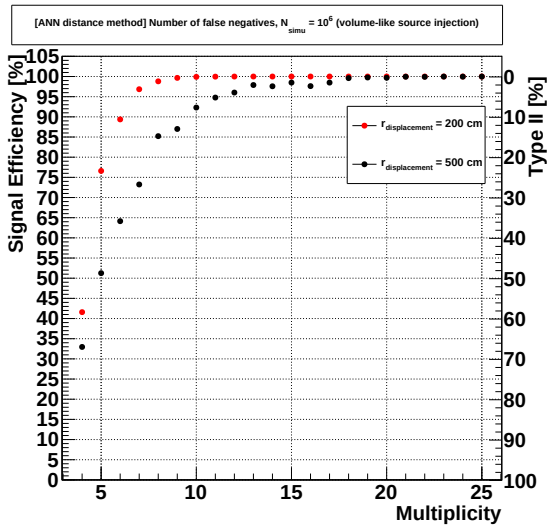

Figure 6.12: Type II error for the ANN distance method based on the injection of line-like background clusters with displacement radius greater than the average lateral development of CR muon-induced showers expected at SK.

Despite the potential improvements in the very-low multiplicity region, the main issues arise when uncorrelated noisy hits are present and are distant from the parent muon track, as in figure 6.1. To this purpose, further MC simulations have been carried out injecting the same line-like source but with one and two events, respectively, generated randomly within the SK volume. The drop of the signal efficiencies in these two cases can be appreciated in the comprehensive figure 6.13 where the performances of all the methods are displayed. It is worth remarking that for multiplicities > 7 the ANN method with a single random hit, performs better than the current SK dimensional fit.

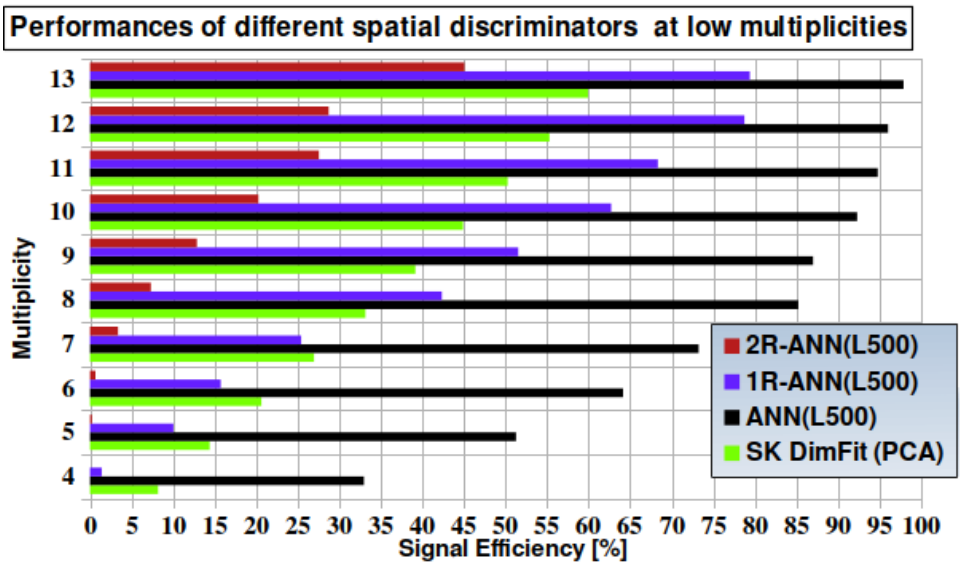

Figure 6.13: Signal efficiencies for the different spallation-like background rejection methods. The number of simulated clusters for each multiplicity is 10^6. The 1-R (and 2-R) notation stands for 1(2) event(s) among the M of the cluster is (are) generated uniformly within the SK volume.

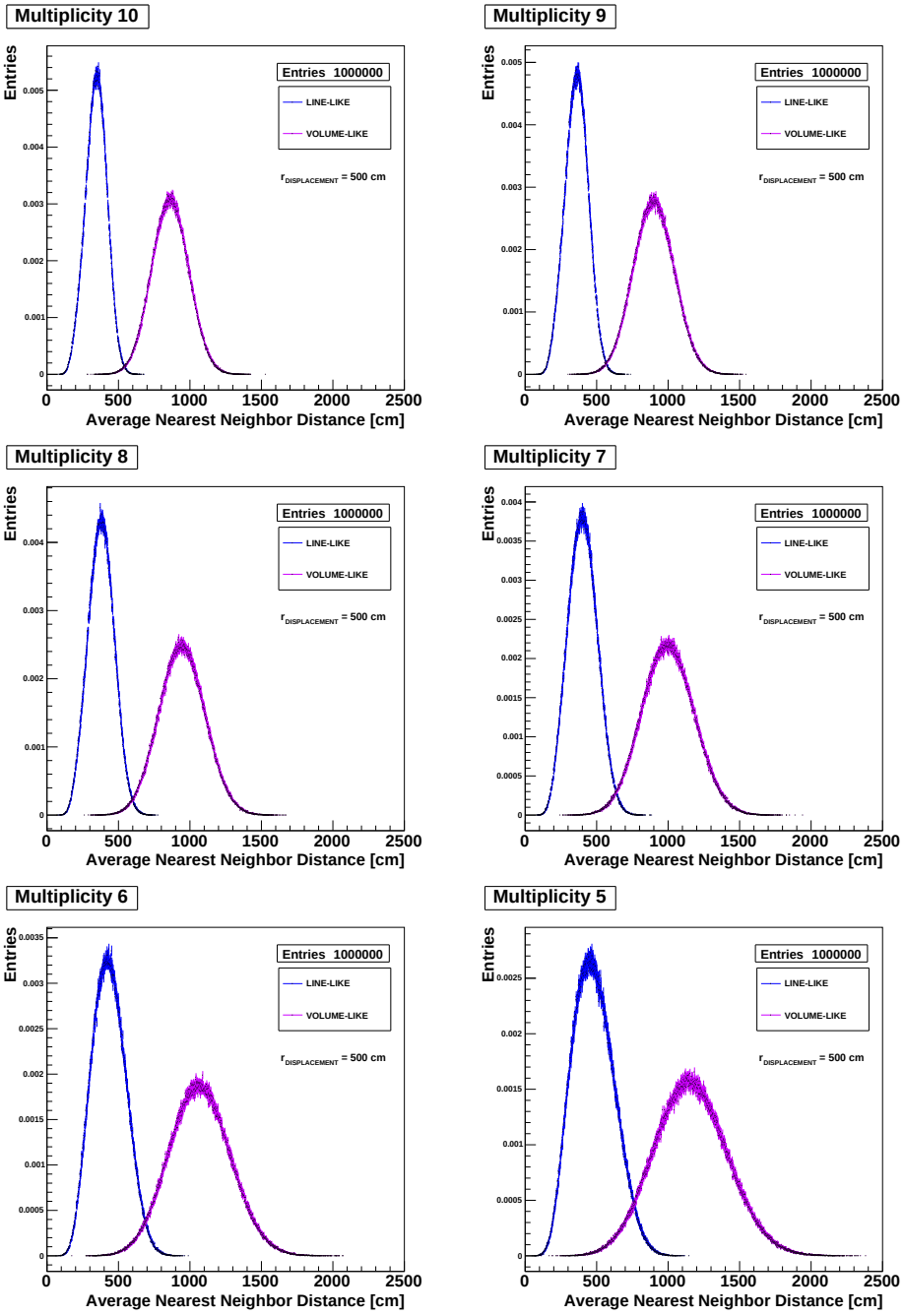

Figure 6.14: ANN distance distributions for volume-like and line-like sources according to different multiplicities.

6.4.4 Final remarks

In analogy with the chapter 5, this final section is devoted to the critical examination of the new proposed topological cut.

The main advantages of the ANN distance method are:

- the topological modelling[14] of the background relies more on its physical origin, *i.e.* mainly from the β-unstable secondaries of the muon-induced showers;
- easy to implement online without additional latencies;
- potential enhancement of the signal efficiencies in the very-low and low multiplicity regimes as demonstrated from the studies with pure line-like clusters.

Conversely, the main drawbacks are:

- full MC studies of the CR muon-induced showers are needed in order to set the MC-driven (or, better, would be data-driven) thresholds and accurately estimate the type I and type II errors. In the case of data-driven thresholds, the ANN distributions of the current silent warnings together with its very low-multiplicity(< 13) extensions might be explored[15] ;
- in the low multiplicity scenario if random hits are present this might affect considerably the choice of the thresholds and therefore the type II error. Thus, after passing the first level trigger based on pure line-like cluster, the human-checking would be mandatory in order to safely broadcast an alert.

[14] it is worth remarking that further improvements might be achieved taken into account the finite longitudinal size of the showers

[15] a proof-of-concept with a small sample of 784 silent warnings has been positively performed. However the main issue in the extension of this analysis is that real-time data are stored only for a limited-time($\sim$ 6 months).

Chapter 7

Conclusions and outlook

In this Thesis the potential improvements of the real-time SN monitor operating at Super-Kamionkade have been studied. To this purpose the work have been structured in two parts.

In the first part new neutrino burst recognition algorithms have been devised and tested in order to extend the horizon visible in real-time, lowering the minimum number of events required for providing an alert within fixed false alarm rate. In particular the different time evolutions of the expected SN signal with respect to the poissonian background has been exploited.

The performance testings with toy MC simulations have shown that the new methods are feasible for the SK SN monitor as well as for other large-scale neutrino detectors partecipating in the SNEWS network. Additionaly it has been demonstrated that they are easy to implement in real-time (also with different clustering algorithms), and they are robust against deviations from the hypothesized (low) poissonian background rate.

Lastly, it is worth mentioning that they are independent on the nature of neutrino cluster and, therefore, it might be used to detect other transient astrophysical objects emitting low-energy neutrino burst.

In the second part, the problem of the non-poissonian component of the SN neutrino background at SK, has been approached. This contribution is mainly due to cosmic ray muon-induced spallation reactions and it is extremly critical in the SK SN monitor since it is the dominant source of background.

After reviewing the current online discrimination techniques, preliminary studies have been carried out in order to reject this component at low multiplicities. To this purpose a new method based on the average nearest neighbor distance analysis of the candidate cluster vertex distribution has been studied with a toy model based on a line-like approximation of the spallation products.

Despite the promising signal-to-noise discrimination achieved with this simplified analysis, full MC studies of the CR muon-induced showers are needed in order to set the proper thresholds and, more importantly, to avoid the issue of the uncorrelated random hits which affects significantly its performances. Additionally, if enough statistics would be available, the setting of a data-driven thresholds could be another way to test the viability of this new method.

Lastly, a 3D event display tool has been designed with the aim to visualize the real and simulated clusters.

In conclusion, since the designed methods are very general, they might be exploited in the following contexts:

- the next Gadolinium phase of the SK supernova monitor. The dissolution of the gadolinium sulfate into the SK water volume will enhance the low-energy antineutrinos detection capabilities (via neutron tagging) but it will change substantially the background behaviour. To this purpose, the full MC simulations of the SN signal and the background with GEANT4 suite will be on order;

- the planned SN monitor system of the future Hyper-Kamiokande detector. This multi-purpose

detector will have a fiducial volume about ten times larger than SK enabling the expansion of the horizon up to $\mathcal{O}(1)$Mpc where CCSNe are supposed to occur on a yearly basis;

- the ongoing SNEWS upgrade(version 2.0) with the aim to increase the probability of observing farther CCSNe improving the current network-based SN alert system.

Appendix A : Neutrino oscillations

If neutrinos are massive, the lepton flavour is not conserved during the neutrino propagation as first pointed out by Bruno Pontecorvo in [34],[35] by analogy with the neutral kaon system.

Let $\nu_i = (\nu_1, \nu_2, \nu_3)$ be the mass eigenstates [1] and $\nu_\alpha = (\nu_e, \nu_\mu, \nu_\tau)$ be the flavour states, the neutrino oscillation formalism links them via the unitary transformation[2]

$$|\nu_\alpha\rangle = \sum_{i=1}^{3} U_{\alpha i} |\nu_i\rangle , \qquad |\nu_i\rangle = \sum_{\alpha=1}^{3} U^*_{\alpha i} |\nu_\alpha\rangle$$

where $U_{\alpha i}$ is the PMNS or the neutrino *neutrino mixing* matrix, by analogy with the CKM matrix in the quark sector.

It is worth noting that the neutrino state evolves in time on the mass basis but the weak interactions occur in the flavour basis, therefore the phase differences induced by neutrino propagation are responsible, as we will see, of the neutrino oscillation in the flavour space.

From the experimental point of view, the measurable quantities are the *survival* and the *disappearance* probabilities of finding the neutrino in the same or different initial flavour state after having crossed a distance L, *i.e.*

$$P_{\alpha\to\beta}(L) = |\langle \nu_\beta | \nu_\alpha(L)\rangle|^2$$

In vacuum

Assuming plane-wave propagation in the z-direction for the mass eigenstate ν_i with the energy E_i

$$|\nu_i(T)\rangle = e^{-ip_i^\mu x_\mu} |\nu_i(0)\rangle$$

in the ultra-relativistic limit, $m \sim 0$ and $L \approx cT$,the probability becomes[3]

$$P_{\alpha\to\beta}(L) = \left| \sum_{i=1}^{3} U_{\alpha i} e^{-i\phi_i(L)} U^*_{\beta i} \right|^2 \tag{1}$$

[1] in the following treatment the minimal hypothesis for the number of *massive* neutrino is assumed, *i.e.* three as the neutrino flavours. Despite more mass eigenstates ($\{\nu_i\}_{i=\{1,\dots,3+n_s\}}$) could exist, the assumption is justified by the fact that such so-called *sterile* neutrinos cannot interact via weak interactions. The general expressions for the neutrino *mixing* are

$$|\nu_\alpha\rangle = \sum_{i=1}^{3+n_s} U_{\alpha i} |\nu_i\rangle , \qquad |\nu_i\rangle = \sum_{\alpha=1}^{3+n_s} U^*_{\alpha i} |\nu_\alpha\rangle$$

[2] *i.e.* the neutrino ν_α produced along with the lepton ℓ_α has flavour state $|\nu_\alpha\rangle$ that is the coherent *linear combinations* of the *mass* eigenstates, *i.e.* (in vacuum) the eigenvalues of the free Hamiltonian operator

$$i\frac{\partial |\nu_i\rangle}{dt} = \hat{\mathcal{H}} |\nu_i\rangle = E_i |\nu_i\rangle$$

[3] in detail, the amplitude is given by

$$\mathcal{A} = \langle \nu_\beta | \sum_{i=1}^{3} U_{\alpha i} e^{-i\phi_i(L)} |\nu_i(0)\rangle = \langle \nu_\beta | \sum_{i=1}^{3} U_{\alpha i} e^{-i\phi_i(L)} \sum_{\sigma=1}^{3} U^*_{\sigma i} |\nu_\sigma(0)\rangle$$

and hence, exploiting the orthogonality $\langle \nu_\beta | \nu_\sigma \rangle = \delta_{\beta\sigma}$, the final result is achieved.

with[4]

$$2\phi_i(L) := p_i^\mu x_\mu(L) \approx (E - p_z)\, L = \frac{(E^2 - p_z^2)}{(E + p_z)} L \approx \frac{m_i^2}{2\,E} L$$

It will prove convenient to take the equation 1 in the form (for the full computations see [32])

$$P_{\alpha\to\beta} = \delta_{\alpha\beta} - 4\sum_{i>j}^{3} \mathfrak{Re}\left(U_{\alpha i}^* U_{\beta i} U_{\alpha j} U_{\beta j}^*\right) \sin^2(\Delta\phi_{ij}) + 2\sum_{i>j}^{3} \mathfrak{Im}\left(U_{\alpha i}^* U_{\beta i} U_{\alpha j} U_{\beta j}^*\right) \sin\left(2\Delta\phi_{ij}\right)$$

where $\Delta\phi_{ij} = \Delta m_{ij}^2 \frac{L}{4E}$, and $\Delta m_{ij}^2 = m_i^2 - m_j^2$ the so-called *mass squared splitting.*

It is worth pointing out that:

- for the antineutrinos

  $$P_{\bar\nu_\alpha\to\bar\nu_\beta} = P_{\nu_\alpha\to\nu_\beta}(U_{\alpha i} \to U_{\alpha i}^*)$$

  and the CP *asymmetry* is defined by[5]

  $$A_{\alpha\beta}^{\mathrm{CP}} = P_{\nu_\alpha\to\nu_\beta} - P_{\bar\nu_\alpha\to\bar\nu_\beta} = 4\sum_{i>j} \mathfrak{Im}\left(U_{\alpha i}^* U_{\beta i} U_{\alpha j} U_{\beta j}^*\right) \sin\left(2\Delta\phi_{ij}\right)$$

- the *survival probability* is given by

  $$P_{\alpha\alpha} = 1 - 4\sum_{i>j}^{3} |U_{\alpha i}|^2 |U_{\alpha j}|^2 \sin^2\left(\Delta\phi_{ij}\right)$$

- in the SI unit

  $$\Delta m^2 \frac{L}{4E} \approx 1.27 \times \left(\frac{\Delta m^2}{\mathrm{eV}^2}\right)\left(\frac{L}{\mathrm{km}}\right)\left(\frac{\mathrm{GeV}}{E}\right)$$

2-flavour case assuming only two mass eigenstates (ν_1 and ν_2), the mixing matrix $U_{\alpha i}$ depends only on the mixing angle θ and, in the case of Majorana neutrino[6] , on the phase parameter φ_1 (which is irrelevant in the probability calculations). The remaining phases can be absorbed by means of the gauge transformations . Therefore, starting from the parametrization

$$U_{\alpha i} = \begin{pmatrix} \cos\theta & \sin\theta \\ -\sin\theta & \cos\theta \end{pmatrix} \begin{pmatrix} 1 & 0 \\ 0 & e^{-i\varphi_1} \end{pmatrix}$$

the *survival probability* becomes

$$\begin{aligned} P_{\alpha\alpha} &= 1 - 4|U_{\alpha 1}|^2 |U_{\alpha 2}|^2 \sin^2\left(\Delta\phi_{12}\right) \\ &= 1 - \sin^2(2\theta)\sin^2\left(\Delta m_{12}^2 \frac{L}{4E}\right) \end{aligned}$$

and, by the complement rule, the *disappereance probability* is

$$P_{\alpha\beta} = \sin^2(2\theta)\sin^2\left(\Delta m_{12}^2 \frac{L}{4E}\right)$$

[4] in this formulation the differences in energy between the mass eigenstates are neglected. The complete treatment requires neutrino wave packets but the final results in terms of probability are basically the same within the experimental resolutions

[5] thus, in disappearance experiment, there is no sensitivity to CP violation ($A_{\alpha\beta}^{\mathrm{CP}} = 0$).

[6] in general, given n-mass eigenstates, the mixing matrix for Dirac and Majorana neutrino are related by

$$U_{\mathrm{Majorana}} = U_{\mathrm{Dirac}} \times \mathrm{diag}(1, \mathrm{e}^{-\mathrm{i}\varphi_1}, \ldots, \mathrm{e}^{-\mathrm{i}\varphi_n})$$

3-flavour case after the absorption of the redundant phases, the standard parametrization of the PMNS matrix is

$$U_{\alpha i}^{PMNS} = \begin{pmatrix} 1 & 0 & 0 \\ 0 & c_{23} & s_{23} \\ 0 & -s_{23} & c_{23} \end{pmatrix} \begin{pmatrix} c_{13} & 0 & s_{13}e^{-i\delta_{\rm CP}} \\ 0 & 1 & 0 \\ -s_{13}e^{i\delta_{\rm CP}} & 0 & c_{13} \end{pmatrix} \begin{pmatrix} c_{12} & s_{12} & 0 \\ -s_{12} & c_{12} & 0 \\ 0 & 0 & 1 \end{pmatrix}$$

where $c_{ij} = \cos\theta_{ij}$ and $s_{ij} = \sin\theta_{ij}$. The 4 free parameters are: the Dirac CP violating phase (δ_{CP}) and the Euler angles (θ_{12}, θ_{23}, θ_{13}). The θ_{12} and θ_{23} are also referred to as *solar* and *atmospheric mixing* angles, respectively.

The other quantities assessable from neutrino oscillation experiment are the two independent *mass-squared splittings* Δm^2_{12} and Δm^2_{3i} where m_1 and m_2 are the closest levels . If ν_3 is the highest mass eigenstate, the mass ordering is referred to as *normal hierarchy* (NH), since the smallest flavour component of ν_3 is ν_e which reminds the mass hierarchy of the charged leptons. Viceversa the *inverted hierarchy*(IH) is when $m_{\nu 3} < m_{\nu 1} < m_{\nu 2}$, where, by convention, $m_{\nu 1} < m_{\nu 2}$. A pictorial representation is displayed in figure 1.

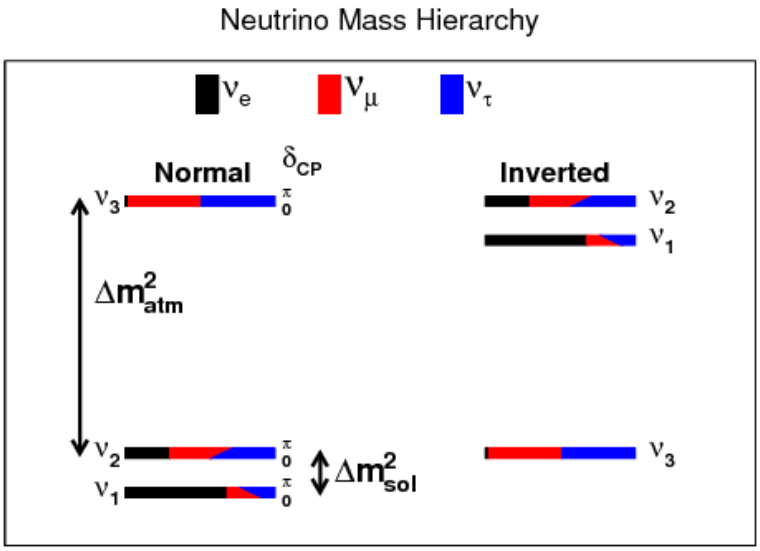

Figure 1: Scheme of the normal and inverted neutrino mass hierarchies with the related flavour components.Figure from[36]

Acknowledgements

At the end, I would like to express my sincere gratitude to Dr. Mathieu Lamoureux for his constant support, kindness, availability, and his valuable advices. Moreover, I would like to say a special thank to him for enduring my poor english during the entire period of this Thesis.

I would also thank Professor Collazuol for his trust in me and for giving me the opportunity to work on this engaging topic within the Super-Kamiokande collaboration.

To this purpose, I would also take advantage of this occasion to express my thanks to professor Koshio-san and to Ikeda-san for the precious discussions and your help.

Furthermore, I would like to thank Fabio Iacob for the good and fruitful conversations in the beginning of my Master Thesis and, above all, during the Bachelor Thesis.

Last but not least, I would like to thank my family and my lovely fiancée Giada for endorsing me in my every life choices.

Bibliography

[1] K. Abe et al. "Real-time supernova neutrino burst monitor at Super-Kamiokande". In: *Astroparticle Physics* 81 (Aug. 2016), pp. 39–48. ISSN: 0927-6505. DOI: 10.1016/j.astropartphys.2016.04.003. URL: http://dx.doi.org/10.1016/j.astropartphys.2016.04.003.

[2] N.Yu. Agafonova et al. "On-line recognition of supernova neutrino bursts in the LVD". In: *Astroparticle Physics* 28.6 (2008), pp. 516–522. ISSN: 0927-6505. DOI: https://doi.org/10.1016/j.astropartphys.2007.09.005. URL: http://www.sciencedirect.com/science/article/pii/S0927650507001284.

[3] E.N. Alekseev et al. "Detection of the Neutrino Signal From SN1987A in the LMC Using the Inr Baksan Underground Scintillation Telescope". In: *Phys. Lett. B* 205 (1988), pp. 209–214. DOI: 10.1016/0370-2693(88)91651-6.

[4] Pietro Antonioli et al. "SNEWS: the SuperNova Early Warning System". In: *New Journal of Physics* 6 (Sept. 2004), pp. 114–114. DOI: 10.1088/1367-2630/6/1/114. URL: https://doi.org/10.1088%2F1367-2630%2F6%2F1%2F114.

[5] Riccardo Barbieri and Rabindra N. Mohapatra. "Limit on the Magnetic Moment of the Neutrino from Supernova 1987A Observations". In: *Phys. Rev. Lett.* 61 (1 July 1988), pp. 27–30. DOI: 10.1103/PhysRevLett.61.27. URL: https://link.aps.org/doi/10.1103/PhysRevLett.61.27.

[6] R.M. Bionta et al. "Observation of a Neutrino Burst in Coincidence with Supernova SN 1987a in the Large Magellanic Cloud". In: *Phys. Rev. Lett.* 58 (1987), p. 1494. DOI: 10.1103/PhysRevLett.58.1494.

[7] A. Burrows. "On detecting stellar collapse with neutrinos". In: *APJ* 283 (Aug. 1984), pp. 848–852. DOI: 10.1086/162371.

[8] Adam Burrows, David Radice, and David Vartanyan. "Three-dimensional supernova explosion simulations of 9, 10, 11, 12, and 13 solar mass stars". In: *Monthly Notices of the Royal Astronomical Society* 485.3 (Feb. 2019), pp. 3153–3168. ISSN: 1365-2966. DOI: 10.1093/mnras/stz543. URL: http://dx.doi.org/10.1093/mnras/stz543.

[9] Adam Burrows, M. Ted Ressell, and Michael S. Turner. "Axions and SN 1987A: Axion trapping". In: *Phys. Rev. D* 42 (10 Nov. 1990), pp. 3297–3309. DOI: 10.1103/PhysRevD.42.3297. URL: https://link.aps.org/doi/10.1103/PhysRevD.42.3297.

[10] C. Casentini et al. "Pinpointing astrophysical bursts of low-energy neutrinos embedded into the noise". In: *Journal of Cosmology and Astroparticle Physics* 2018.08 (Aug. 2018), pp. 010–010. ISSN: 1475-7516. DOI: 10.1088/1475-7516/2018/08/010. URL: http://dx.doi.org/10.1088/1475-7516/2018/08/010.

[11] Edward L. Chupp, W. Thomas Vestrand, and Claus Reppin. "Experimental Limits on the Radiative Decay of SN 1987A Neutrinos". In: *Phys. Rev. Lett.* 62 (5 Jan. 1989), pp. 505–508. DOI: 10.1103/PhysRevLett.62.505. URL: https://link.aps.org/doi/10.1103/PhysRevLett.62.505.

[12] Amol S. Dighe and Alexei Yu. Smirnov. "Identifying the neutrino mass spectrum from a supernova neutrino burst". In: *Phys. Rev. D* 62 (3 July 2000), p. 033007. DOI: 10.1103/PhysRevD.62.033007. URL: https://link.aps.org/doi/10.1103/PhysRevD.62.033007.

[13] S. Fukuda et al. "The Super-Kamiokande detector". In: *Nuclear Instruments and Methods in Physics Research A* 501.2 (Apr. 2003), pp. 418–462. DOI: 10.1016/S0168-9002(03)00425-X.

[14] W. Fulgione, N. Mengotti-Silva, and L. Panaro. "Neutrino burst identification in underground detectors". In: *Nuclear Instruments and Methods in Physics Research Section A: Accelerators, Spectrometers, Detectors and Associated Equipment* 368.2 (1996), pp. 512–516. ISSN: 0168-9002. DOI: https://doi.org/10.1016/0168-9002(95)00672-9. URL: http://www.sciencedirect.com/science/article/pii/0168900295006729.

[15] Todd Haines et al. "Neutrinos From SN1987A in the Imb Detector". In: *Nucl. Instrum. Meth. A* 264 (1988). Ed. by K.C. Wali, pp. 28–31. DOI: 10.1016/0168-9002(88)91097-2.

[16] Alexander Himmel and Kate Scholberg. "Supernova Neutrino Detection". In: *Nuclear and Particle Physics Proceedings* 273-275 (Apr. 2016), pp. 1897–1901. DOI: 10.1016/j.nuclphysbps.2015.09.306.

[17] K. Hirata et al. "Observation of a Neutrino Burst from the Supernova SN 1987a". In: *Phys. Rev. Lett.* 58 (1987). Ed. by K.C. Wali, pp. 1490–1493. DOI: 10.1103/PhysRevLett.58.1490.

[18] Shunsaku Horiuchi and James P Kneller. "What can be learned from a future supernova neutrino detection?" In: *Journal of Physics G: Nuclear and Particle Physics* 45.4 (Mar. 2018), p. 043002. ISSN: 1361-6471. DOI: 10.1088/1361-6471/aaa90a. URL: http://dx.doi.org/10.1088/1361-6471/aaa90a.

[19] M. Ikeda et al. "Search for Supernova Neutrino Bursts at Super-Kamiokande". In: *The Astrophysical Journal* 669.1 (Nov. 2007), pp. 519–524. ISSN: 1538-4357. DOI: 10.1086/521547. URL: http://dx.doi.org/10.1086/521547.

[20] Hans-Thomas Janka. "Neutrino Emission from Supernovae". In: *Handbook of Supernovae* (2017), pp. 1575–1604. DOI: 10.1007/978-3-319-21846-5_4. URL: http://dx.doi.org/10.1007/978-3-319-21846-5_4.

[21] Hans-Thomas Janka. "Neutrino-Driven Explosions". In: *Handbook of Supernovae* (2017), pp. 1095–1150. DOI: 10.1007/978-3-319-21846-5_109. URL: http://dx.doi.org/10.1007/978-3-319-21846-5_109.

[22] M. Kachelriess et al. "Exploiting the neutronization burst of a galactic supernova". In: *Phys. Rev. D* 71 (2005), p. 063003. DOI: 10.1103/PhysRevD.71.063003. arXiv: astro-ph/0412082.

[23] E. Kolbe, K. Langanke, and P. Vogel. "Estimates of weak and electromagnetic nuclear decay signatures for neutrino reactions in Super-Kamiokande". In: *Phys. Rev. D* 66 (1 July 2002), p. 013007. DOI: 10.1103/PhysRevD.66.013007. URL: https://link.aps.org/doi/10.1103/PhysRevD.66.013007.

[24] Shirley Weishi Li and John F. Beacom. "First calculation of cosmic-ray muon spallation backgrounds for MeV astrophysical neutrino signals in Super-Kamiokande". In: *Physical Review C* 89.4 (Apr. 2014). ISSN: 1089-490X. DOI: 10.1103/physrevc.89.045801. URL: http://dx.doi.org/10.1103/PhysRevC.89.045801.

[25] Shirley Weishi Li and John F. Beacom. *Spallation Backgrounds in Super-Kamiokande Are Made in Muon-Induced Showers*. 2015. arXiv: 1503.04823 [hep-ph].

[26] Shirley Weishi Li and John F. Beacom. "Tagging spallation backgrounds with showers in water Cherenkov detectors". In: *Physical Review D* 92.10 (Nov. 2015). ISSN: 1550-2368. DOI: 10.1103/physrevd.92.105033. URL: http://dx.doi.org/10.1103/PhysRevD.92.105033.

[27] Wan Linyan. "Experimental Studies on Low Energy Electron Antineutrinos and Related Physics". PhD thesis. Tsinghua University, 2018.

[28] N. B. Linzer and K. Scholberg. "Triangulation pointing to core-collapse supernovae with next-generation neutrino detectors". In: *Physical Review D* 100.10 (Nov. 2019). ISSN: 2470-0029. DOI: 10.1103/physrevd.100.103005. URL: http://dx.doi.org/10.1103/PhysRevD.100.103005.

[29] William J. Marciano and Zohreh Parsa. "Neutrino electron scattering theory". In: *J. Phys. G* 29 (2003), pp. 2629–2645. DOI: 10.1088/0954-3899/29/11/013. arXiv: hep-ph/0403168.

[30] Jost Migenda. "Supernova Model Discrimination with Hyper-Kamiokande". In: (2020). arXiv: 2002.01649 [astro-ph].

[31] Alessandro Mirizzi et al. "Supernova Neutrinos: Production, Oscillations and Detection". In: 39 (July 2015). DOI: 10.1393/ncr/i2016-10120-8.

[32] Spandan Mondal. "Physics of Neutrino Oscillation". In: (Nov. 2015). arXiv: 1511.06752 [hep-ph].

[33] Ken'ichiro Nakazato et al. "SUPERNOVA NEUTRINO LIGHT CURVES AND SPECTRA FOR VARIOUS PROGENITOR STARS: FROM CORE COLLAPSE TO PROTO-NEUTRON STAR COOLING". In: *The Astrophysical Journal Supplement Series* 205.1 (Feb. 2013), p. 2. ISSN: 1538-4365. DOI: 10.1088/0067-0049/205/1/2. URL: http://dx.doi.org/10.1088/0067-0049/205/1/2.

[34] B. Pontecorvo. "Mesonium and anti-mesonium". In: *Sov. Phys. JETP* 6 (1957), p. 429.

[35] B. Pontecorvo. "Neutrino Experiments and the Problem of Conservation of Leptonic Charge". In: *Sov. Phys. JETP* 26 (1968), pp. 984–988.

[36] X. Qian and P. Vogel. "Neutrino mass hierarchy". In: *Progress in Particle and Nuclear Physics* 83 (July 2015), pp. 1–30. ISSN: 0146-6410. DOI: 10.1016/j.ppnp.2015.05.002. URL: http://dx.doi.org/10.1016/j.ppnp.2015.05.002.

[37] Karolina Rozwadowska, Francesco Vissani, and Enrico Cappellaro. "On the rate of core collapse supernovae in the milky way". In: *New Astronomy* 83 (Feb. 2021), p. 101498. ISSN: 1384-1076. DOI: 10.1016/j.newast.2020.101498. URL: http://dx.doi.org/10.1016/j.newast.2020.101498.

[38] Katsuhiko Sato and Hideyuki Suzuki. "Analysis of neutrino burst from the supernova 1987A in the Large Magellanic Cloud". In: *Phys. Rev. Lett.* 58 (25 June 1987), pp. 2722–2725. DOI: 10.1103/PhysRevLett.58.2722. URL: https://link.aps.org/doi/10.1103/PhysRevLett.58.2722.

[39] K. Scholberg. "The SuperNova Early Warning System". In: *Astronomische Nachrichten* 329.3 (Mar. 2008), pp. 337–339. ISSN: 1521-3994. DOI: 10.1002/asna.200710934. URL: http://dx.doi.org/10.1002/asna.200710934.

[40] Jonathon Shlens. *A Tutorial on Principal Component Analysis*. 2014. arXiv: 1404.1100 [cs.LG].

[41] Michael Smy. "Low Energy Event Reconstruction and Selection in Super-Kamiokande-III". In: *30th International Cosmic Ray Conference*. Vol. 5. July 2007, pp. 1279–1282.

[42] Maurizio Spurio. *Probes of Multimessenger Astrophysics: Charged cosmic rays, neutrinos, γ-rays and gravitational waves*. Springer, 2018. DOI: 10.1007/978-3-319-96854-4.

[43] Alessandro Strumia and Francesco Vissani. "Precise quasielastic neutrino/nucleon cross-section". In: *Phys. Lett. B* 564 (2003), pp. 42–54. DOI: 10.1016/S0370-2693(03)00616-6. arXiv: astro-ph/0302055.

[44] Irene Tamborra. "Supernova Neutrinos: New Challenges and Future Directions". In: *Journal of Physics: Conference Series* 888 (Sept. 2017), p. 012040. DOI: 10.1088/1742-6596/888/1/012040.

[45] T. Totani et al. "Future Detection of Supernova Neutrino Burst and Explosion Mechanism". In: *The Astrophysical Journal* 496.1 (Mar. 1998), pp. 216–225. DOI: 10.1086/305364. URL: https://doi.org/10.1086%2F305364.

[46] Chenyuan Xu. "Study of neutrino signal from astronomical object in Super-Kamiokande". PhD thesis. Okayama University, 2019.